DESIGN OPTIMIZATION AND CONTROL OF A PARALLEL LOWER-ARM EXOSKELETON

by

RAMAZAN ÜNAL

Submitted to the Graduate School of Engineering and Natural Sciences
in partial fulfillment of
the requirements for the degree of
Master of Science

Sabancı University

Spring 2008

DESIGN OPTIMIZATION AND CONTROL OF A
PARALLEL LOWER-ARM EXOSKELETON

APPROVED BY

Assist. Prof. Dr. Volkan PATOĞLU .....
(Thesis Supervisor)

Assoc. Prof. Dr. Erhan BUDAK .....

Assist. Prof. Dr. Güllü KIZILTAŞ .....

Assist. Prof. Dr. Kemallettin ERBATUR .....

Assoc. Prof. Dr. Mustafa ÜNEL .....

DATE OF APPROVAL: .....

to my family

&

beloved aunt

Acknowledgements

I would very much like to acknowledge my supervisor Professor Volkan Patoğlu for his great support, unlimited patience, and tolerance. He extended my engineering knowledge and made drastic contributions to my background. I learned how to become a researcher thanks to him and my academic career will go further level with his guidance and great efforts. In addition to being my mentor, he helped me to get thorough hard times like my friend with his great understanding at these complicated situations and thanks to him we worked like a colleague. I hope we will keep this collaboration continuing for other projects in the future.

I also would like to acknowledge Professor Güllü Kızıltaş, for her help and support on my study. I also would like to express my appreciation and sincere gratitude to the other members of my committee, Professor Mustafa Ünel, Professor Kemalettin Erbatur, Professor Ahmet Onat and Professor Erhan Budak for their involvement and generous contributions of guidance.

I also would like to thank all of my friends in the Mechatronics Engineering program for their sincere friendship. Especially, I would like to acknowledge my friends in Human-Machine Interaction laboratory, Ahmetcan Erdoğan, Hakan Kapson, and Ayşe Neşe Tüfekçiler, for their support and collaborations in our projects and studies. I would like to express my appreciation to Neşe once again, since she spared her time and helped me with patience on the CAD drawings of the system.

I also would like to thank my family for their support, love and unlimited patience during my entire life. They always trust me unreservedly and encourage me to go further level in my career.

I gratefully acknowledge the support by TÜBİTAK-BİDEB with research fellowship.

DESIGN OPTIMIZATION AND CONTROL OF A
PARALLEL LOWER-ARM EXOSKELETON

Ramazan Ünal

ME MS Thesis, 2008

Thesis Supervisor: Assist. Prof. Volkan Patoğlu

Keywords: Lower-arm exoskeleton, multi-critera design optimization, parallel mechanisms, position and impedance control of force feedback devices.

Abstract

Wearable force feedback robotic devices, *haptic exoskeletons*, are becoming increasingly common as they find widespread use in medical and virtual reality (VR) applications. Allowing users to mechanically interact with computationally mediated environments, haptic exoskeletons provide users with better "immersion" to VR environments.

Design of haptic exoskeletons is a challenging task, since in addition to being ergonomic and light weight, such devices are also required to satisfy the demands of any ideal force-feedback device: ability withstand human applied forces with very high stiffness and capacity to display a full range of impedances down to the minimum value human can perceive. If not properly designed by taking these conflicting requirements into account, the interface can significantly deteriorate the transparency of displayed forces; therefore, the choice of the kinematic structure and determination of the dimensions of this kinematic structure have significant impacts on the overall performance of any haptic display independent of the control algorithm employed.

In this thesis, we first propose a general framework for optimal dimensional synthesis of haptic interfaces, in particular for haptic interfaces with closed kinematic chains, with respect to multiple design objectives. We identify and categorize the relevant performance criteria for the force feedback exoskeletons and address the

trade-offs between them, by applying a Pareto-front based multi-objective design optimization procedure. Utilizing a fast converging gradient-based method, the proposed framework is computational efficient. Moreover, the approach is applicable to any set of performance indices and extendable to include any number of design criteria.

Subsequently, we extend this framework to assist the selection of the most appropriate kinematic structure among multiple mechanisms. Specifically, we perform a rigorous comparison between two spherical parallel mechanisms (SPMs) that satisfy the ergonomic necessities of a human forearm and wrist and select the kinematic structure that results in superior performance for force-feedback applications. Utilizing the Pareto optimal set of solutions, we also assign dimensions to this mechanism to ensure an optimal trade-off between global kinematic and dynamic performance.

Following the design optimization phase, we perform kinematic and dynamic analyses of the SPM-based exoskeleton in independent coordinates to facilitate efficient simulation and real-time implementation of model based controllers. We decide on the hardware components considering human wrist torque and force limits, safety and ergonomy constraints, and present the CAD model of a prototype of the exoskeleton. Finally, we implement model based task-space position and impedance controllers in simulation and present the results of them.

PARALLEL MEKANİZMA TABANLI ALT KOL DIŞ İSKELETİNİN KONTROLÜ VE TASARIM ENİYİLEŞTİRMESİ

Ramazan Ünal

ME Master Tezi, 2008

Tez Danışmanı: Yrd. Doç. Dr. Volkan Patoğlu

Anahtar Kelimeler: Alt kol dış iskeleti, çok-kriterli tasarım eniyileştirmesi, paralel mekanizmalar, kuvvet geri-beslemeli robotların pozisyon ve empedans kontrolü.

Özet

Giyilebilir kuvvet yansıtımlı robotlar, haptik dış iskeletler, medikal ve sanal gerçeklik uygulamalarında geniş kullanım alanı bulduklarından, günümüzde oldukça yaygınlaşmaya başlamışlardır. Haptik dış iskeletler, bilgisayarda oluşturulmuş ortamlarla kullanıcıların mekanik etkileşimine izin vererek onların sanal gerçeklik ortamına daha iyi dahil olabilmelerini sağlamaktadırlar.

Haptik dış iskeletlerin tasarımı oldukça zorlu bir görevdir, zira bu cihazların, ergonomi ve hafiflik kriterlerinine ek olarak, ideal herhangi bir kuvvet yansıtımlı makinadan beklenen özellikleri de sağlaması gerekmektir; insan tarafından uygulanan kuvvetlere çok yüksek katılıkla dayanabilmeli, ayrıca insanın algılayabileceği minimum empedansa kadar inebilen tam impedans aralığını sergileyebilme kapasitesine sahip olmalıdır. Robot, bu birbiriyle çelişen gereklilikler göz önünde bulundurularak tasarlanmazsa, cihazın kendisi yansıtılan kuvvetlerin şeffaflığını önemli ölçüde bozabilir. Bu yüzden, kinematik yapının seçimi ve boyutlarının belirlenmesinin, uygulanan kontrol algoritmasından bağımsız olarak, herhangi bir haptik yansıtımın genel performansında önemli etkileri vardır.

Bu tezde, ilk olarak haptik aygıtların, özellikle kapalı kinematik yapıdakilerin, birden çok tasarım amacına göre optimum boyut sentezinde kullanılabilecek genel bir şablon sunuyoruz. Kuvvet yansıtımlı dış iskeletelerle ilgili performans kriterlerini belirleyip, sınıflandırıyoruz ve Pareto-front bazlı çok amaçlı tasarım en iyileştirmesi

prosedürünü kullanarak aralarındaki ödünleşimi ifade ediyoruz. önerilen çerçeve, hızlı yakınsayan gradient bazlı bir metod kullandığından, hesaplama açısından verimlidir. Ayrıca, bu yaklaşım seçilen performans kriterlerinden bağımsız olup, istenilen sayıda tasarım kriteri için kullanılabilir.

Ardından, bu çerçeveyi en uygun kinematik yapının seçimine yardımcı olacak şekilde genişletiyoruz. özel olarak, insan ön kolu ve bileğinin ergonomik ihtiyaçlarını karşılayan iki küresel paralel mekanizmanın (KPM) titiz bir biçimde kıyaslanmasını gerçekleştirip, kuvvet yansıtımlı uygulamalarda daha iyi performans sergileyen kinematik yapıyı seçiyoruz. Ayrıca seçilen mekanizma için, Pareto eğrisindeki en iyi tasarımların bulunduğu kümeden, kinematik ve dinamik performanslar arasındaki optimum ödünleşimi sağlayan mekanizma boyutlarını belirliyoruz.

Tasarım en iyileştirilmesi aşamasını takiben, model bazlı kontrolörlerin benzetim ve gerçek zamanlı uygulamalarını verimli olarak gerçekleştirebilmek için KPM bazlı dışiskeletin kinematik ve dinamik analizlerini, bağımsız kordinatlarda yapıyoruz. ınsan bileğinin tork ve kuvvet sınırlarını göz önünde bulundurarak donanım bilesenlerine karar verip, ilk prototip dış iskeletin tasarım modelini sunuyoruz. Son olarak, model bazlı görev alanı pozisyon ve empedans tipi kontrolörlerin benzetimlerini uygulayıp, sonuçlarını sunuyoruz.

Table of Contents

List of Figures

List of Tables

Chapter 1

Introduction

Wearable force feedback robotic devices, *haptic exoskeletons*, are becoming increasingly common as they find widespread use in medical and virtual reality (VR) applications. Allowing users to mechanically interact with computationally mediated environments, haptic exoskeletons provide users with better "immersion" to VR environments.

Design of haptic exoskeletons is a challenging task, since in addition to being ergonomic and light weight, such devices are also required to satisfy the demands of any ideal force-feedback device: ability to withstand human applied forces with very high stiffness and capacity to display a full range of impedances down to the minimum value human can perceive.

If not properly designed, the dynamics of an exoskeleton device can significantly deteriorate the transparency of displayed forces during haptic rendering of virtual environments. Even though parasitic effects due to the device dynamics can be actively compensated using feedback paradigms, such approaches require use of force sensors. Active cancelation approaches suffer from the limited bandwidth of the force sensors, undesired sensor dynamics, sensor actuator non-collocation, and high cost of force sensors. Design optimization studies performed on haptic interfaces can shape the device dynamics in a favorable manner; therefore, these studies can have a significant impact on the overall performance of the haptic display independent of the control algorithm employed.

Multiple performance requirements have to be considered *simultaneously* while performing design optimization of haptic exoskeletons. Since the performance with respect to many of these criteria cannot be improved without deteriorating others,

design trade-offs are inevitable. Determination of an optimal design with respect to many criteria is a difficult problem and should be handled with formal multi-objective optimization methods that assign trade-offs systematically.

Besides the important task of determining the most appropriate dimensions of a given parallel mechanism architecture that constitute the best compromise between multiple performance criteria, another relevant concern during design optimization studies is the selection of the most appropriate kinematic structure. Selection of the most appropriate kinematic structure for a given task is non-trivial, since kinematics and dynamics of each mechanism may differ substantially from each other and intuitive approaches may fail to capture the important trade-offs among multiple mechanisms.

Finally, hardware implementation and real-time controls of parallel mechanism based exoskeleton devices pose some important challenges. Selection of actuators and transmission mechanism are critical for the kinematic, kinetic, and dynamic performance of high-fidelity impedance display type devices. Efficient formulation of the kinematics and dynamics models of parallel mechanisms is essential to ensure high real-time control loop rates required by force feedback applications.

1.1 Objectives

The objectives of this thesis are to design an optimal lower-arm exoskeleton to serve as a high-fidelity haptic interface, manufacture its prototype, and perform kinematic and dynamic analyses of the exoskeleton for implement real-time position and impedance controllers implementations.

The major goals of the thesis can be listed as follows:

- Identify relevant performance criteria for force-feedback exoskeleton devices,
- Build an efficient and general framework for multi-criteria design optimization and comparison of parallel mechanisms based robotic devices,
- Employ the framework for multi-criteria design optimization of spherical parallel mechanisms and decide on the superior kinematic structure and optimal dimensions of a lower-arm exoskeleton to serve as a high-fidelity haptic interface,
- Decide on the hardware components and control architecture of the lower-arm exoskeleton to satisfy safety and performance limitations,
- Perform kinematic and dynamic analyses of the device for simulation and real-time controls implementation,

1.2 Overview of the Proposed Approaches and the Structure of the Document

Chapter II presents a general framework for optimization of haptic interfaces, in particular for haptic interfaces with closed kinematic chains, with respect to multiple design objectives, namely kinematic and dynamic criteria. Both performance measures are discussed and optimization problems for a haptic interface with best worst-case kinematic and dynamic performance are formulated. Non-convex single objective optimization problems are solved with a branch-and-bound type (modified culling) algorithm. Pareto methods characterizing the trade-off between multiple design criteria are advocated for multi-criteria optimization over widely used scalarization approaches and Normal Boundary Intersection method is applied to efficiently obtain the Pareto-front hyper-surface. The framework is applied to a sample parallel mechanism (five-bar mechanism) and the results are compared with the results of previously published methods in the literature. Finally, dimensional synthesis of a high performance haptic interface utilizing its Pareto-front curve is demonstrated.

Chapter III presents multi-criteria design optimization of a parallel mechanism based force-feedback exoskeleton for human forearm and wrist. Relevant design objectives for force-feedback exoskeleton devices are identified and categorized. Rigorous comparison of two spherical parallel mechanisms that satisfy the ergonomic necessities of a human forearm and wrist is presented, by extending a Pareto front based multi-criteria optimization framework developed for parallel mechanisms. The kinematic structure that results in superior performance for force-feedback applications is selected. Subsequently, dimensional synthesis is performed for this spherical parallel mechanism to ensure an optimal trade-off between global kinematic and dynamic performance of the exoskeleton device.

Chapter IV presents design, dynamic modeling, instrumentation, and simulations of position and impedance controllers of a four degree-of-freedom parallel forearm and wrist exoskeleton device, designed to serve as a high-quality impedance display. The kinematic structure and dimensions of the device are optimized with respect to kinematic and dynamic performance criteria to ensure that the device is isotropic, can achieve high position and force bandwidths, can accommodate most

of the natural workspace of human forearm and wrist in a singularity-free manner. Direct drive actuation is preferred during implementation of the device to satisfy high stiffness, low friction, and no backlash. Dynamic simulations of the device are completed to allow selection of actuators that can withstand a reasonable percentage of human joint torques. To ensure high control loop rates, real-time solutions of configuration and motion level forward and inverse kinematics of the device are addressed and computationally efficient formulation of the dynamics model of the parallel mechanism is implemented using Kane's method. Model based task-space position controllers as well as task-space impedance controllers are simulated and results are presented.

Finally, Chapter V summarizes the contributions, discusses future work and concludes the thesis.

Chapter 2

A Multi-criteria Design Optimization Framework for Parallel Robots

Robotic manipulators with parallel kinematic chains are becoming increasingly common due to the inherent advantages they offer with respect to their serial counterparts. Parallel mechanisms possess compact designs with high stiffness and have low effective inertia since their actuators can be grounded in many cases. In terms of dynamic performance, high position and force bandwidths are achievable with parallel mechanisms thanks to their light but stiff structure. Besides, parallel mechanisms do not superimpose position errors at joints, hence can achieve high precision.

Since the performance of parallel mechanisms is highly sensitive to their dimensions, design optimization studies are absolutely necessary for these types of mechanisms [46]. Design optimization studies of such mechanisms with closed kinematic chains are significantly more challenging than serial ones. Parallel mechanisms have smaller workspace with possible singularities within the workspace and their analysis is considerably harder than the analysis of mechanisms with serial kinematic chains. Due to the additional complexities involved, the dimensional synthesis of parallel mechanisms is still an active area of research.

Optimum design of parallel mechanisms even for a single objective function is challenging due to the nonlinear, large scale nature of such mechanisms [38] and non-convex properties of performance indices with respect to the design variables [49]. Many different optimization approaches applicable to nonlinear, non-convex optimization problems such as genetic algorithms [38, 58, 71], simulated annealing [51], Bayesian techniques [58, 59], Monte-Carlo simulations [58, 71], controlled randomized searches [43], performance charts [41], workspace atlases [42], and branch and

bound methods [57] have been applied to design optimization of parallel mechanisms. In general, deterministic methods can get stuck at a local optimum, heuristic methods cannot guarantee optimality of the converged solution, while branch and bound type methods are only as accurate as the discretization selected.

While performing dimensional synthesis of parallel mechanisms, various performance criteria such as kinematic and dynamic isotropy, stiffness, sensitivity, and transmission capability have to be considered *simultaneously*. The performance with respect to many of these criteria cannot be improved without deteriorating others; hence, design trade-offs are inevitable. Determination of optimal dimensions with respect to many design criteria is a difficult problem and should be handled with multi-objective optimization methods so that trade-offs can be assigned in a systematic manner.

As emphasized earlier, an optimal design of a haptic interface can only be achieved by considering many competing objectives. There exists several studies in which multiple design criteria have been addressed for this purpose. Hayward *et al.* define the relationship between multiple criteria and utilize sensitivities of these criteria to conduct a hierarchical optimization study [20]. Multiple objectives are considered sequentially in [1, 33, 51, 57] by searching for parameter sets resulting in near optimal kinematic performance and then selecting the design exhibiting the best dynamic performance from this reduced parameter space. Task-priority [7], probabilistic weighting [45], composite index [36], and tabular methods [68] are among the other approaches that consider multiple criteria.

Even though these studies can account for multiple design criteria, they can be broadly classified under *scalarization methods* in which the multi-criteria optimization problem is addressed in an indirect manner, by first transforming it into a (or a series of) single objective (scalar) problem(s). These approaches either aggregate multiple criteria into a single objective function through some form of weighting or prioritize one objective and select others to serve as constraints to form a single objective optimization model. Scalarization methods possess the inherent disadvantage of their aggregate objective functions requiring preferences or weights to be determined apriori, *i.e.* before the results of the optimization process are actually known [12]. Since assigning proper weights or prioritizing different criteria is a prob-

lem dependent, non-trivial task, these techniques fall short of providing a general framework to the design of parallel mechanisms.

Pareto methods, on the other hand, incorporate all optimization criteria within the optimization process and address them simultaneously to find a set of efficient solutions. Each design alternative in the solution set corresponds to a non-dominated design in the objective space. In other words, these methods aim to construct the Pareto-front hyper-surface representing the design trade-offs between multiple criteria. Once such a hyper-surface resolving the design trade-offs is obtained, an appropriate design on this hyper-surface can be selected taking into account other design requirements of the particular application in consideration. Pareto methods allow the designer to make an informed decision by studying a wide range of options, since they contain solutions that are optimum from an *overall* standpoint; unlike aggregate optimization techniques that may ignore this trade-off viewpoint. Thanks to this feature, Pareto methods are better suited as a general solution framework for design optimization of parallel mechanisms. Pareto methods provide a better understanding of the optimization problem allowing all the consequences of a decision with respect to all the objectives be explored.

Due to its transparent interpretation even for non-expert users, the most commonly used technique for generating points on the Pareto-front hyper-surface is to solve for optimal solutions of (convex) weighted sums of several objective functions for various different settings of weights [29, 31]. This traditional approach is an extension of the scalarization approaches and suffers from two major drawbacks: Weighted sum approach does not guarantee a uniform spread of Pareto points for an even spread of weights, and this approach cannot solve for points on the non-convex portions of the Pareto-front hyper-surface [10]. Without prior knowledge of the shape of the Pareto-front hyper-surface, it is not possible to estimate values of weights that map out a uniform spread of points on the Pareto-front hyper-surface, while increasing the number of weights does not result in points on the non-convex portions of the Pareto set. Therefore, ill-behaved nature of the weighted sum approach frequently results in under-represented regions of the Pareto-front hyper-surface and cause selection of an inferior design solution by failing to map important non-dominated ones.

Other methods exists in literature that directly attacks the problem to solve for the Pareto set. As regards to employing these Pareto methods for design of parallel mechanisms, Krefft *et al.* recently applied a modified genetic algorithm (GA) to a problem with multiple objective functions and solved for the Patero-front hyper-surface [35, 34]. Similarly in [56], GA is applied to multi criteria optimization of a 2-DoF parallel robot. Despite their inherent advantage of resulting in multiple non-dominated design solutions within a single optimization search, GA approaches suffer from several disadvantages. Specifically, the convergence performance of GA is highly dependent on user-specified parameters such as sharing factor, and the results are very sensitive to these user specified parameters. Moreover, GA methods demand inferior computational cost with increasing number of objective functions, hence cannot be easily adopted or scaled for use of more than two objective functions [8]. More importantly, GA might prematurely converge to sub-optimal solutions [22]. Finally, use of GAs to obtain Pareto front hyper-surface has the disadvantages of large computational expense as well as a tendency for clumping of solutions in objective space resulting in under-represented regions of the Pareto-front [12].

Finally, in [60] authors proposed a multi-objective design framework for optimization of parallel mechanisms based on Normal Boundary Intersection (NBI) method [11]. In [62] the proposed framework is applied to design of a 3RPS-R type robot for dual purpose application. The proposed framework is computational efficient, applicable to any set of performance indices, and extendable to include any number of design criteria that is required by the application.

In this Chapter, the framework first introduced by the authors in [60, 61] is further studied and extended results are presented. Global kinematic and dynamic performance of parallel mechanisms over a pre-defined singularity free workspace are maximized simultaneously and the Pareto-front curve for these two criteria is obtained. Firstly, the global solutions of non-convex min-max performance criteria are solved independently from each other using a modified branch and bound algorithm, called culling algorithm [57]. Once optimal solutions of each single criteria optimization problem are obtained, Normal Boundary Intersection (NBI) method [11], which performs a deterministic geometric search within the objective space, is utilized to efficiently compute uniformly distributed design solutions on the Pareto-front curve.

The proposed framework is applicable to other performance indices and easily extendable to include further design criteria that may be required by the application. The results are compared against sequential optimization and weighted sum approaches. To facilitate the determination of the "best" solution of the Pareto set, estimation of the relative weights of performance indices that are implicit in the Pareto plot is demonstrated.

This Chapter is organized as follows: Section 2.1 discusses several kinematic and dynamic performance measures, while Section 2.2 introduces the sample mechanism used for the analysis, a 2-DoF parallel five-bar linkage. Section 2.3 formulates the multi-criteria optimization problem. Section 2.4 explains the optimization methods used to address the single and multi-criteria optimization problems and is followed by results and their discussion in Section 2.5. Section 2.6 presents conclusions and future work. Kinematic and dynamic analyses of a five-bar linkage are detailed in the Appendix A.

2.1 Measuring Kinematic and Dynamic Performance

Since design of a mechanism cannot be apart from its application field, as a sample task, both kinematic and dynamic performance of parallel mechanisms are to be optimized to achieve force feedback devices with low parasitic effects. A *haptic interface* is a computer-controlled motorized device that physically interacts with a human operator to render presence of computationally mediated environments. An ideal haptic device is desired to withstand human applied forces with very high stiffness and be capable of displaying a full range of impedances down to the minimum value human can perceive. The performance of a haptic interface under closed loop control is measured by the *transparency* of the display, that is, by quantifying the match between the desired and actually rendered impedance values. During haptic rendering, the haptic interface is coupled to the control system and its existence results in parasitic effects on the displayed impedances, deteriorating the perfect transparency. Low effective inertia is crucial, especially while rendering impedance values at the lower end of the spectrum. Even though inertia cancelation can be

implemented in control, issues like sensor and quantization noise limit the applicability of these approaches. A haptic interface with isotropic performance is also of interest, since such a design will result in a more uniform "feel" of the device throughout the workspace, while simultaneously making most efficient use of the available actuators. Therefore, independent of the control algorithm used, both the kinematic and dynamic performance of the haptic device have an impact on the overall performance of the haptic display.

To quantify performance, several design matrices, including kinematic Jacobian and mass matrices, are studied and to date, many scalar performance indices have been proposed. These indices either represent a distance to a singular configuration or quantify the directional independence (uniformity) of configuration dependent design matrices. Since singular values of a matrix provide a versatile metric to quantify its properties, most of the indices are derived as a function of these values.

To measure kinematic performance, properties of the kinematic Jacobian matrix (J) are studied thoroughly. *Condition number*, proposed by Salisbury and Craig [53], describing the worst-case behavior at a given configuration is one of the most commonly used kinematic performance measures. Given as the ratio of the minimum and maximum singular values of the kinematic Jacobian matrix, this measure locally characterizes directional isotropy for both force/motion transmission accuracy and actuator utilization of a manipulator. Condition number is *local* measure of kinematic performance; therefore, is not constant over the entire workspace. Extensions of this index have been proposed to characterize the performance of a manipulator over the entire workspace. Gosselin and Angeles proposed *global* condition indices based on integral of local kinematic performance measures over the workspace [17].

In this Chapter, a global performance index is chosen to quantify the kinematic isotropy of the five-bar mechanism since the objective of the design problem is to minimize the parasitic effects of the manipulator over the workspace. Even though any global index can be utilized within the framework presented, to allow comparisons with earlier published results the global isotropy index ($\mathcal{GII}$), introduced in [57] by Stocco *et al.*, is preferred. $\mathcal{GII}$ is a workspace inclusive worst-case kinematic performance measure that is intolerant of poor performance over the entire workspace. $\mathcal{GII}$ is calculated as the ratio of the minimum of smallest singular

value and maximum of largest singular value of the kinematic Jacobian matrix over the workspace. As a global worst case performance measure, maximizing $\mathcal{GII}$ corresponds to designing a mechanism with best worst-case kinematic performance. Moreover, an optimal $\mathcal{GII}$ results in a uniform kinematic Jacobian matrix for the sake of precision, while also increasing the efficiency of utilization of the actuators. $\mathcal{GII}$ can be mathematically expressed as

$$GII = min_{\boldsymbol{\gamma}_0, \boldsymbol{\gamma}_1 \in W} \frac{\underline{\sigma}(J(\boldsymbol{\alpha}, \boldsymbol{\gamma}_0))}{\overline{\sigma}(J(\boldsymbol{\alpha}, \boldsymbol{\gamma}_1))} \tag{2.1}$$

where J represents the kinematic Jacobian of the manipulator, $\underline{\sigma}$ and $\overline{\sigma}$ are the smallest and the largest singular values of the kinematic Jacobian matrix, $\boldsymbol{\gamma_0}$ and $\boldsymbol{\gamma_1}$ are the configurations in the workspace that result in the extreme singular values, $\boldsymbol{\alpha}$ is the column matrix of design variables, and W represents the workspace.

Dynamic performance is measured in a similar manner to the kinematic performance, but this time properties of the inertia matrix (M) capturing the relation between actuator force/torque and end-effector acceleration, are studied. The goal for improving dynamic performance is to minimize inertia effects that conflict with high acceleration demands. To characterize *local* dynamic performance Asada defined the effective inertia matrix expressing the homogeneity of the moment of inertia of the non-redundant manipulators and introduced the concept of generalized inertia ellipsoid [2]. Yoshikawa proposed a dynamic manipulability measure [69], which is an extension of manipulability concept and measures the degree of arbitrariness in changing end-effector accelerations. Similar to the case of local kinematic performance indices, extensions to local dynamic indices have been proposed to characterize the performance of a manipulator over the entire workspace.

In this study, to be consistent with the metric chosen for the kinematic performance, the workspace inclusive best worst-case performance measure, global dynamic index ($\mathcal{GDI}$) [57], is used to quantify dynamic performance. $\mathcal{GDI}$ measures the largest effect of mass on the dynamic performance by calculating the maximum largest singular value over the workspace of the effective inertia matrix at the end-effector and is computed as inverse of this maximum of largest singular value. Hence, $\mathcal{GDI}$ quantifies the global worst-case performance of a manipulator. Maximizing $\mathcal{GDI}$ results in reduced maximum largest singular value of the effective inertia matrix, decreasing the inertial interference by the system. $\mathcal{GDI}$ can be

mathematically expressed as

$$GDI = min_{\boldsymbol{\gamma} \in W} \frac{1}{1 + \overline{\sigma}(M(\boldsymbol{\alpha}, \boldsymbol{\beta}, \boldsymbol{\gamma}))} \tag{2.2}$$

where M represents effective inertia matrix of the manipulator as seen at the end effector, $\overline{\sigma}$ is the largest singular value of the effective inertia matrix, $\boldsymbol{\gamma}$ is the configuration in the workspace that results in the largest singular value, $\boldsymbol{\alpha}$ is the column matrix of design variables, and W represents the workspace.

As mentioned earlier, the framework introduced in this Chapter allows for study of the mechanisms with respect to any performance index that is of interest to the designer. In this study, $\mathcal{GII}$ and $\mathcal{GDI}$ are selected as the performance criteria so that comparisons with earlier published results can be undertaken.

In general, since entries of kinematic Jacobian and inertia matrices may not be homogenous in units, proper normalization is necessary such that the measures defined on these matrices are meaningful. Among several approaches proposed in literature, normalization with a characteristic length [30, 33] or a nominal link length [36], and partitioning the matrices into translational and rotational parts [33, 38] are the most popular choices. Normalization is not necessary for the sample problem presented in this Chapter, as it possesses only a translational workspace.

2.2 Five-Bar Linkage

The optimization framework presented in this Chapter is applied to a 2-DoF five-bar parallel mechanism due its sufficient richness with relative simplicity allowing better interpretation of the optimization problem at hand. Moreover, scalarization/aggregrate methods have been applied to the multi-criteria optimization of this mechanism in the literature, rendering comparisons of different approaches possible. The methods discussed in this Chapter constitute a general framework for design optimization of parallel mechanisms and is by no means limited to the sample mechanism studied.

A five-bar mechanism can be characterized by lengths l_0, l_1 , l_2, l_3 and l_4 of its five links and three variables r, γ and ν defining the position and orientation of its workspace as shown in Figure 2.1. To quantify the orientation of each link, joint

angles q_i ($i = 1..4$) measured from the x-axis are introduced. A five-bar mechanism with symmetric link lengths ($l_1 = l_4$, $l_2 = l_3$) and a symmetric workspace that is located parallel to the x and y-axes of the global coordinate system ($\gamma = \pi/2$, $\nu = \pi/2$) is selected in this study. Moreover, out of four possible assembly configurations, only the elbow-out posture, as depicted in Figure 2.1, is studied. Optimality of the above listed decisions in terms of both kinematic and dynamic performance have already been shown in the literature [57].

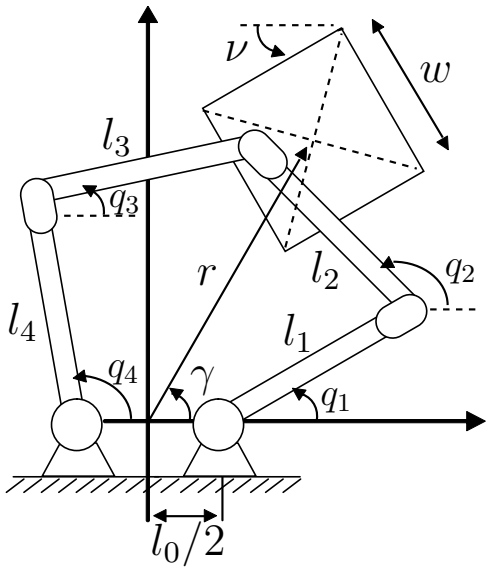

Figure 2.1: Five-bar mechanism in the elbow-out posture

Assuming that the dimension of the symmetric workspace w is pre-determined, the optimization problem can be formulated using four design variables: l_0, l_1, l_2 and r. Table 2.1 presents the design variables $\boldsymbol{\alpha}$ and design parameters $\boldsymbol{\beta}$ (parameters that do not change during the design process) for the symmetric five-bar mechanism.

Kinematic and dynamic models of the symmetric parallel five-bar mechanism are detailed in the Appendix A, along with the Jacobian and inertia matrices to be used during the design optimization.

2.3 Optimization Problem

Two objective functions characterizing the kinematic and dynamic performances of the mechanism are considered in this Chapter. To quantify the kinematic/dynamic performance of the parallel mechanism global isotropy index ($\mathcal{GII}$) and global dy-

Table 2.1: Design variables $\boldsymbol{\alpha}$ and parameters $\boldsymbol{\beta}$

	Symbol	**Definition**	**Unit**
α_1	l_0	Distance between actuated joints	mm
α_2	l_1, l_4	Length of actuated links	mm
α_3	l_2, l_3	Length of free links	mm
α_4	r	Workspace center position	mm
β_1	$w = 100$	Workspace side length	mm
β_2	$\gamma = 90°$	Angle between r and x-axis	$^\circ$
β_3	$\nu = 90°$	Angle between W and y-axis	$^\circ$

namic index ($\mathcal{GDI}$) [57], are chosen. Both of these indices are conservative workspace inclusive worst-case performance measures that are intolerant of poor performance over the entire workspace. An optimal $\mathcal{GII}$ results in a uniform kinematic Jacobian matrix, while optimizing $\mathcal{GDI}$ minimizes the effective inertia matrix of the system. Since the stiffness of the system is dominated by the compliance of the transmission and actuators, a Jacobian matrix with high isotropy not only results in the uniform kinematic behavior but also maximizes the stiffness of the device.

The objective of optimization is to maximize the worst kinematic isotropy of the mechanism ($\mathcal{GII}$) while simultaneously minimizing the effective inertia (max singular value of the effective inertia matrix or $\mathcal{GDI}$). The negative null form of the multi-objective optimization problem can be stated as

$$\begin{aligned} max \;\; & \mathbf{F}(\boldsymbol{\alpha}, \boldsymbol{\beta}, \boldsymbol{\gamma}) \\ & \mathbf{G}(\boldsymbol{\alpha}, \boldsymbol{\beta}) \leq 0 \\ & \boldsymbol{\alpha}_l < \boldsymbol{\alpha} < \boldsymbol{\alpha}_u \end{aligned} \tag{2.3}$$

where $\mathbf{F}$ represents the column matrix of objective functions that depend on the design variables $\boldsymbol{\alpha}$, parameters $\boldsymbol{\beta}$, and workspace positions $\boldsymbol{\gamma}$. Symbol $\mathbf{G}$ represents the inequality constraint functions that also depend on design variables and parameters. Finally, $\boldsymbol{\alpha}_l$ and $\boldsymbol{\alpha}_u$ correspond to the lower and upper bounds of the design variables, respectively.

For the symmetric five-bar mechanism in elbow out posture, the column matrices

$\mathbf{F}$ and $\mathbf{G}$ can be explicitly derived as

$$\mathbf{F} = \begin{bmatrix} \mathcal{GII} \\ \mathcal{GDI} \end{bmatrix}, \mathbf{G} = \begin{bmatrix} (l_0/2 + w/2)^2 + (r + w/2)^2 - (l_1 + l_2)^2 \\ -q_2 \\ q_2 - q_1 \end{bmatrix}$$

In these expressions, the first element of the $\mathbf{G}$ matrix constrains the design space to ensure a closed kinematic chain throughout the reachable workspace while last two elements stand for the elbow-out posture. Note that the constraint equations are smooth; hence, they are suitable for use with gradient based optimization approaches.

2.4 Methods

In the previous section, the formulation for the multi-criteria optimization problem for best worst-case performance of a haptic interface is described. Before addressing the multi-criteria optimization problem, the nature of the problem with respect to the selected performance criteria is to be studied. Inspecting the performance criteria, one can conclude that both $\mathcal{GII}$ and $\mathcal{GDI}$ are non-convex with respect to the design variables. Moreover, as workspace inclusive measures, their calculation requires searches over the workspace. As discussed in the introduction, several methods have been proposed to solve for the single criteria optimization problem of parallel manipulators. In general, descent methods suffer from getting trapped at local optima while heuristic methods cannot guarantee optimality of their solution. Feasibility and efficiency of a branch-and-bound type method, called *culling algorithm*, is advocated in the literature to address single objective min-max problems [57].

In this study, the culling algorithm is used to independently solve for the optimum designs with respect to $\mathcal{GII}$ and $\mathcal{GDI}$. The culling algorithm improves the computational efficiency of a brute-force method by reducing (culling) the amount of searches required through effective performance comparisons. The algorithm capitalizes on the fact that as a worst-case measure, once the global performance index for certain reference parameters is calculated conducting a search over the entire workspace, reduction of the feasible parameter set can be performed without per-

forming any other searches over the workspace. Specifically, after a global index value is calculated for the reference parameters, comparisons with local indices at *only* a single configuration in the workspace can be overtaken. Hence, searches over workspace is significantly reduced as they are conducted only when it is necessary to calculate new reference global index values. Comparing all set of design variables to find the best worst-case index, the algorithm will converge to an optimum solution within the discretization accuracy. As the culling method substantially reduces the amount of workspace searches required by a brute-force method, it is a fast and efficient algorithm to address min-max type problems.

Since the performance of the culling algorithm is highly dependent on the initial reference values assigned, a fast gradient-based optimization method, sequential quadratic programming (SQP), is used to solve for a local extrema that will serve as a good initialization value. This modification applied to the initialization of the culling algorithm increases the computational efficiency by resulting in a higher culling rate at the first iteration. Once a solution is obtained, another SQP is invoked to converge to a guaranteed optima within the discretization region.

If the multi-criteria optimization problem is treated as multiple single objective problems where objective functions are handled independently, optimal solution for one criteria may result in an unacceptable design for the other. To achieve a "best" solution with respect to multiple criteria, the trade-off between objectives needs to be quantified. Scalarization approaches assumes apriori knowledge of this trade-off and converts the multi-criteria problem into a single objective one by assigning proper weights or priorities to each performance index. On the other hand, Pareto methods do not require any apriori knowledge about the design trade-offs and solve for the locus of all dominant solutions with respect to multiple objective functions, constituting the so-called the Pareto-front hyper-surface. Hence, designers can make a more realistic choice between multiple "best" solutions and avoid the challenge of synthetically ranking their preferences.

There exists several methods to obtain the Pareto-front hyper-surface, among which Normal Boundary Intersection (NBI) method is one of the most featured. As the Pareto-front hyper-surface is a geometric entity in the objective space forming the boundary of feasible region, NBI approach attacks the *geometric problem* di-

rectly by solving for single-objective constrained subproblems to obtain uniformly distributed points on the hyper-surface. NBI solves for subproblems which only depend on the defined optimization model, that is, chosen objective functions and design constraints since these equations map the feasible design space onto the attainable objective space. Given independent optimal solutions for each objective function (solutions of each single objective problem), called shadow points, NBI first constructs an hyper-plane in the objective space by connecting these shadow points with straight lines. Then, this hyper-plane is divided into grids that control the resolution of solutions on the Pareto-front hyper-surface. For each point on the grid, a geometric subproblem is solved to find the *furthest* point on the line that extends along the surface normal passing through the grid point and is in the feasible domain of the objective space. Hence, NBI obtains the Pareto-front with reducing the problem to many single-objective constrained subproblems. Number of subproblems can be adjusted by defining resolution of the grid that maps to the number of points on the Pareto-front hyper-surface. As the number of points increases, the computational time increases linearly, but since the method assumes spatial coherence and uses solution of a subproblem to initialize the next subproblem, convergence time for each subproblem may decrease resulting in further computational efficiency.

For a Pareto-front generation method can be classified as a "good" one, the following criteria are to be satisfied [72]: minimum distance of the Pareto-front hyper-surface produced by the algorithm should be low with respect to the true Pareto-front hyper-surface and the maximum spread of solutions as well as maximum number of elements on the Pareto optimal set should be high.

NBI method results in exceptionally uniform distributed points on the Pareto-front hyper-surface without requiring any tuning of the core algorithm. Moreover, once shadow points are obtained, NBI solves for the geometric problem directly utilizing a fast converging gradient-based method, evading the computationally demanding aggregate optimization problems required in for most of the scalarization methods. Therefore, NBI method promises to be much faster and efficient than other methods to obtain a well represented Pareto-front hyper-surface including aggregate methods such as weighted sums and evolutionary optimization approaches such as GAs.

It should also be noted that the NBI method can solve for points on the non-convex regions of Pareto-front hyper-surfaces, a feature that is missing from the weighted sum methods. Compared to weighted sum techniques, NBI achieves higher solution efficiency as it does not suffer from clumping of solution in the objective space. NBI is also advantageous over other methods as it trivially extends to handle any number of objective functions. Compared to Multi-Objective Genetic Algorithm (MOGA) [14] that requires problem dependent fitness and search related tuning and several steps to reach convergence, a standard NBI approach can map the Pareto-front hyper-surface with higher accuracy and uniformity, while also inheriting the efficiency of gradient-based methods.

Relying on gradient techniques, NBI assumes sufficient smoothness of the geometric problem at hand, but it has also been demonstrated that the method performs remarkably well even for non-smooth geometries [50]. In the presence of non-continuous regions, multiple initializations of the NBI method may be required for efficiently generating the Pareto-front hyper-surface. For the case of strongly discontinuous geometries, hybridization with MOGA-II to supply feasible initialization points at each continuous sub-region can be employed, as proposed in [50]. It is noted that since NBI relies on equality constraints, it is possible for NBI not to find a solution on the true Pareto-front hyper-surface, converging to a local optima. In such a case, post processing on the solutions of NBI subproblems can be employed to filter out undesired dominated solutions.

2.5 Results and Discussion

Table 2.2 presents the results of the modified culling algorithm for the single objective problems, for best kinematic and dynamic isotropy, respectively. These results are obtained by conducting a global search over the entire parameter space with discretization step sizes of 2 mm and 1 mm for the parameter space and workspace, respectively, and by further improving on these results through several local searches with finer discretizations at the neighborhood of the results suggested by the global searches.

Figure 2.2 presents the change of singular values over the workspace for the

Table 2.2: Results of independent optimizations with respect to $\mathcal{GII}$ and $\mathcal{GDI}$.

	Best Design for Kinematic Isotropy	**Best Design for Dynamic Isotropy**	**Unit**
$\mathcal{GII}$	0.783	0.407	–
$\mathcal{GDI}$	0.622	0.766	–
l_0	0.4	0.1	mm
l_1	299.7	89.9	mm
l_2	300.0	115.2	mm
r	419.6	123.6	mm

optima of single objective problems. Subfigures 2.2(a) and 2.2(c) pertain to the best kinematic design while Subfigures 2.2(b) and 2.2(d) belong to best dynamic design. Results indicate that best design with respect to solely $\mathcal{GII}$ suffers from poor dynamic performance, while best design with respect to only $\mathcal{GDI}$ possesses poor kinematic performance.

To characterize the trade-off between the single objective solutions, Pareto-front curve for the bi-objective optimization problem is constructed in Figure 2.3. Two different techniques are employed to form the Pareto-front curve, namely NBI method and aggregated performance index method. For the NBI method, a grid size of ten points are selected. In Figure 2.3 the distribution of these points on the Pareto-front curve is marked by dots. For the second method, an aggregated performance index ($\mathcal{API}$) is defined as the weighted linear combination of $\mathcal{GII}$ and $\mathcal{GDI}$. In particular, $API = \lambda\, GII + (1-\lambda)\, GDI$, where $0 \leq \lambda \leq 1$ denotes the weighting factor. Nine aggregated optimization problems are solved for ten equally spaced weighting factors utilizing the modified culling algorithm with discretization step sizes of 5mm for the parameter space and 1mm for the workspace. Circles in the Figure 2.3 denote the distribution of aggregate solutions on the Pareto-front curve and are labeled with their corresponding weighting factor.

As expected, NBI method generates a very uniform distribution of points on the Pareto-front curve while the solutions of the aggregate problem are clumped at certain locations of the curve. To obtain a uniform distribution using the aggregated index approach, proper weights should be assigned to ensure uniform distribution.

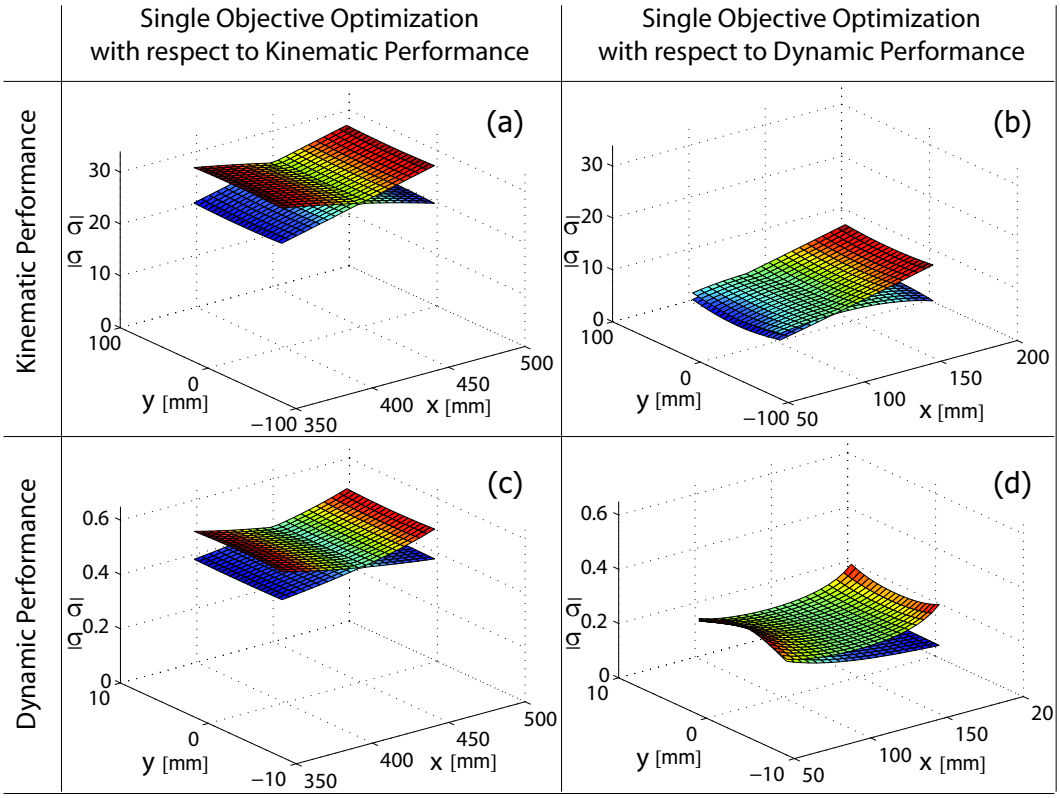

Figure 2.2: Change of singular values over the workspace for the optima of single objective problems. Subfigures (a) and (c) pertain to the best kinematic design, while (b) and (d) belong to the best dynamic design.

However, the characteristics of the weight distribution is not known before the problem is solved. Moreover, since the aggregate performance index relies on the relatively costly culling algorithm to solve for each point on the Pareto-front curve, its accuracy is limited by the computationally feasible discretization step size. In the Figure 2.3, aggregate problem results in identical solutions for different weighting factors, particulary for weighting factors $\lambda = 0.4$ to $\lambda = 0.5$, $\lambda = 0.6$ to $\lambda = 0.7$, and $\lambda = 0.8$ to $\lambda = 0.9$, respectively, since a course discretization step size is chosen so that computations can be completed in a reasonable amount of time. As this problem suggests, solving for each aggregate performance index at each weighting is a computationally demanding task, limiting the density of feasible discretization. NBI method possesses an inherent advantage in terms of computational cost, as it attacks the direct geometric problem to obtain the Pareto-front curve and utilizes continuous, computationally efficient gradient methods for the solution.

In addition to the efficiency offered via the uniform distribution of solutions on

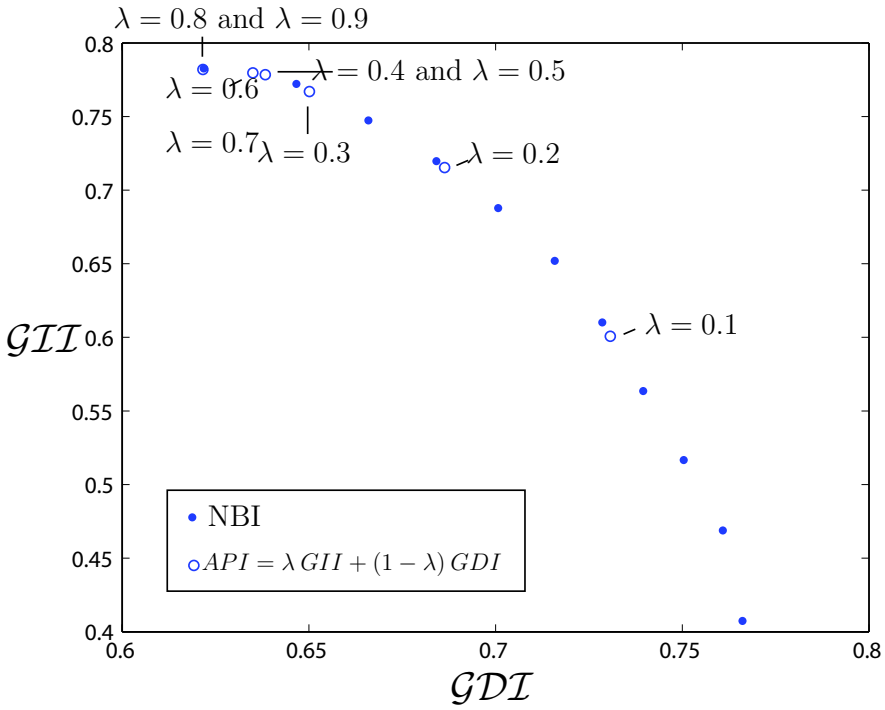

Figure 2.3: Comparison of NBI and aggregated performance index methods. Symbol λ is the weighting factor.

the Pareto-front curve, NBI approach results in *orders of magnitude* improvement in the computation time, especially for the design problem at hand, as depicted in Figure 2.4. All of the simulations presented in Figure 2.4 are performed using a 32 bit Windows XP workstation that is equipped with a 3.40GHz Intel Xeon processor with 1MB L2 cache and 4GB DDR-2 400MHz SDRAM.

As can be observed from Figure 2.4, the aggregate problem scales exponentially with the discretization step size, rendering an accurate solution of even nine points on the Pareto-curve almost impossible for the simple sample problem at hand. On the other hand, NBI method solves for points on the Pareto-front curve very effectively, in about 1/14 time of the weighted-sum approach with course (5mm) step size. The accuracy of solutions obtained by the NBI method is dependent on a parameter that adjuts the constraint tolerance for the algorithm. Figure 2.5 illustrates that the convergence of NBI method is acceptable with all reasonable values of such tolerance. Particularly, Figure 2.5 presents solutions obtained using the NBI approach with three different tolerance values: 10^{-7}, 10^{-8}, and 10^{-9}. Since NBI employs a local search algorithm that is dependent on the initial conditions, con-

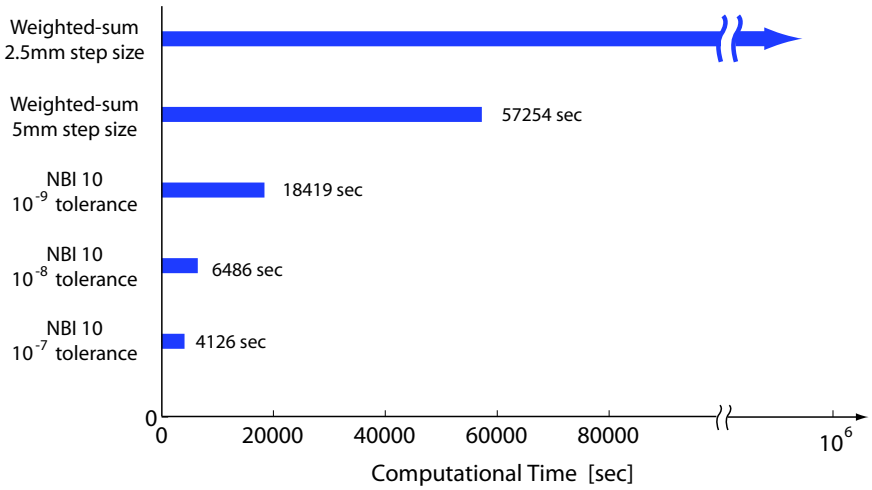

Figure 2.4: Computational effort of NBI method with respect to different tolerances and weighted sum method with respect to different discretizations.

vergence can be poor at certain trials as can be observed for two dominated points in Figure 2.5. However, poor convergence of certain points is not an uncorrectable drawback, as solution for those points can be repeated with closer initializations and tighter tolerances. The computational time for NBI method scales linearly with tolerance values as it does with number of points selected for the grid.

To allow for comparisons of the proposed approach with other scalarization methods in the literature, sequential optimizations are implemented for the sample problem. In the first sequential approach (SA1), parameter sets resulting in the best $\mathcal{GII}$ values for each discrete value of the parameter r are calculated. The change in $\mathcal{GII}$ values and the link lengths are plotted in Figure 2.6 with respect to the independent parameter r. In this plot, one can observe that $\mathcal{GII}$ value increases monotonically with increasing r until the link length l_1 reaches its allowable upper limit (300 mm) while link lengths l_0 and l_2 also increase with increasing r until l_2 reaches its allowable upper limit (300 mm). Once l_2 reaches its upper limit, monotonic decrease in l_0 values can be observed until l_1 reaches its upper limit.

Similarly for the second sequential approach (SA2), parameter sets resulting in the best $\mathcal{GDI}$ values for each discrete value of the parameter r are calculated. The change in $\mathcal{GDI}$ values and the link lengths are plotted in Figure 2.7 with respect to the independent parameter r. In this plot, one can observe that $\mathcal{GDI}$ value increases for a while as the link lengths increase and after attaining its maximum

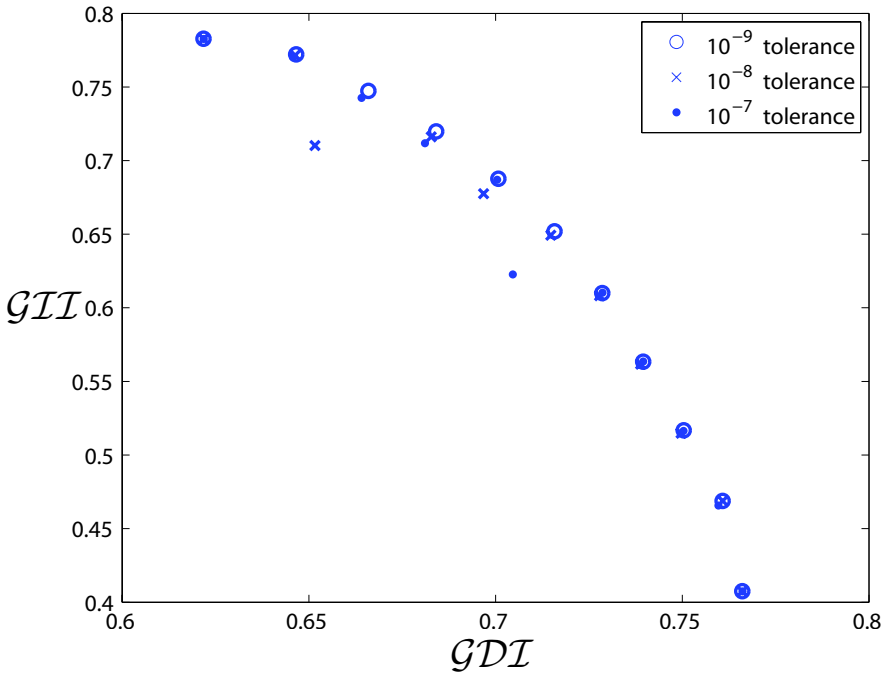

Figure 2.5: Distribution NBI solutions with three different tolerances: 10^{-7}, 10^{-8}, and 10^{-9}.

value $\mathcal{GDI}$ decreases monotonically. The increase in $\mathcal{GDI}$ with the increasing link lengths take place due to the fact that $\mathcal{GDI}$ is a measure of effective inertia of the system, over which the kinematic Jacobian of the mechanism has high influence. At the low values of r, effects of kinematic Jacobian (hence the link lengths) dominate over the effects of link inertias and $\mathcal{GDI}$ increases with the link lengths. At around $r = 80mm$, the effects of link inertias become more dominant and the expected trend of decrease of $\mathcal{GDI}$ with increasing link lengths is observed. The optimal link lengths of the mechanism are highly affected by the upper limits. When link length l_2 reaches its allowable upper limit (300 mm), l_1 starts a rapid increase until it encounters its own upper limit (300 mm). Similarly, link lengths l_0 which stays very low up until l_2 reach its limit, starts increasing until l_1 reaches its upper limit, at which point l_0 experiences a sharp decrease.

Assigning r as the independent variable, the SA1 (SA2) uses the set of "optimal" solutions with respect to $\mathcal{GII}$ ($\mathcal{GDI}$) as the feasible search domain to conduct another single criteria optimization, this time with respect to $\mathcal{GDI}$ ($\mathcal{GII}$). In other words, the parameter set resulting in the best $\mathcal{GDI}$ ($\mathcal{GII}$) value is selected from the Figure 2.6 (Figure 2.7). The results of the sequential optimization approaches are

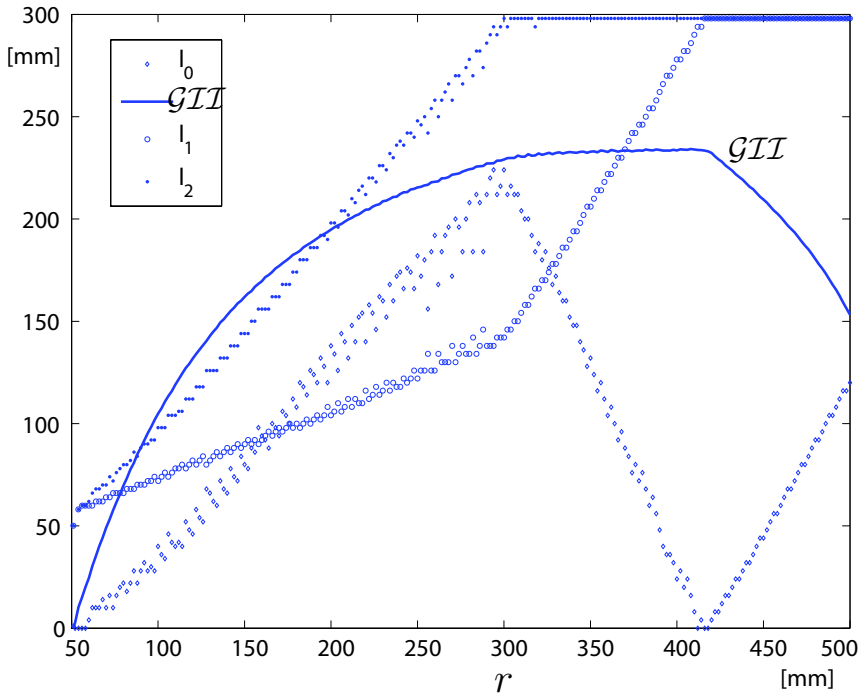

Figure 2.6: Parameter sets with best $\mathcal{GII}$ values for each discrete value of r.

plotted in Figure 2.8 with respect to a dense Pareto-curve obtained using the NBI approach. Inspecting the plot, one can conclude that the "best" solutions obtained using the sequential optimization approaches are both *dominated* – are points not lying on the Pareto front, meaning there exists solutions for which one can improve $\mathcal{GII}$ ($\mathcal{GDI}$) while keeping $\mathcal{GDI}$ ($\mathcal{GII}$) constant or vice versa. In fact, regrading to the solution of SA1 improvements up to 20% in the $\mathcal{GII}$ value and up to 3% in the $\mathcal{GDI}$ value are possible by choosing one of the designs that lies on the Pareto-front boundary found by the intersection of the Pareto curve and vertical and horizontal line, respectively, passing through that point. Similarly, improvements up to 20% in the $\mathcal{GII}$ value and up to 16% in the $\mathcal{GDI}$ value are possible for solution calculated by SA2.

As emphasized earlier, any point on the Pareto-front curve is a non-dominated solution. Hence it is up to the designer to choose the "best" design for the application at hand, considering the characteristic of the trade-off mapped out by the Pareto-front boundary. This decision may be challenging since the relative weights are not transplant, but implicit in the Pareto plot. For the convex portions of the Pareto-front curve, it is always possible to estimate the relative weight λ of the ob-

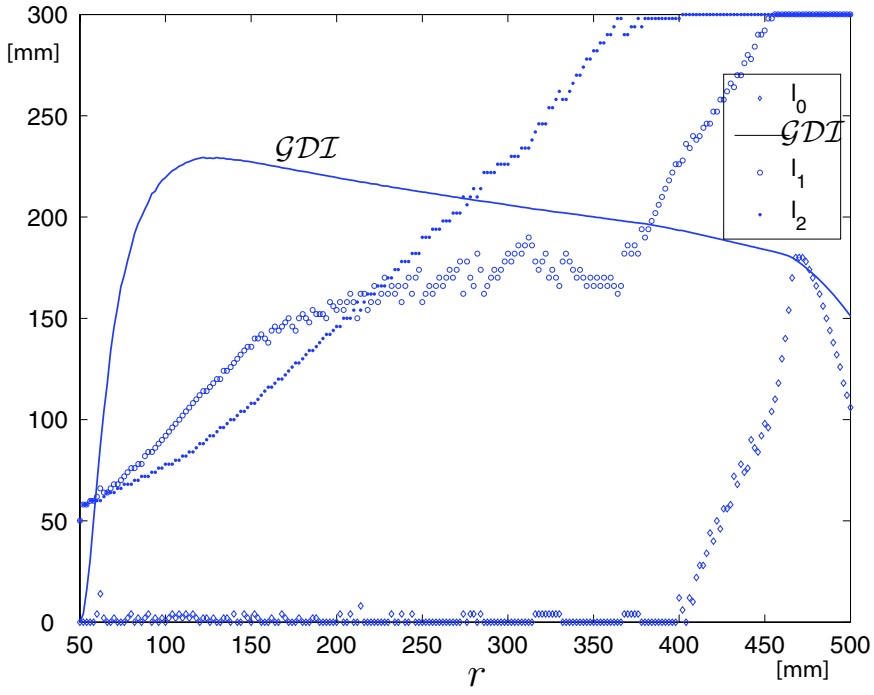

Figure 2.7: Parameter sets with best $\mathcal{GDI}$ values for each discrete value of r.

jective functions since there exists an explicit relationship between the slope of the Pareto curve at a Pareto point and λ [10]. Reflecting the relative importance (preference) among the objective functions under consideration, weights help negotiating the decision trade-offs within the Pareto set. Note that, in contrast to the weighting sum approach, within the proposed framework the weights are obtained after the points representing the Pareto set are solved for. With such an approach the weights of points that are uniformly spread on the Pareto-front curve can trivially be constructed, a task that is not feasible with weighted sum approaches.

To estimate the weights of points on the Pareto set, a polynomial of 5^{th} order is fitted with $R^2 = 0.9985$ on the points obtained using NBI method as shown in Figure 2.9. Given the slope (θ) of this curve at any point, relative weight λ of the objective functions can be estimated as $\lambda = 1/(1-\theta)$.

The Pareto methods not only allow additional constraints be considered for the final decision but also let the designer adjust these constraints while simultaneously monitoring their effect on the set of non-dominated solutions. For the sample problem analyzed, a design is selected by imposing two additional physical constraints on the Pareto-front curve: a limit on the allowable workspace and a limit on the actuator size. Assuming that motors with 40mm diameter will be used as the actu-

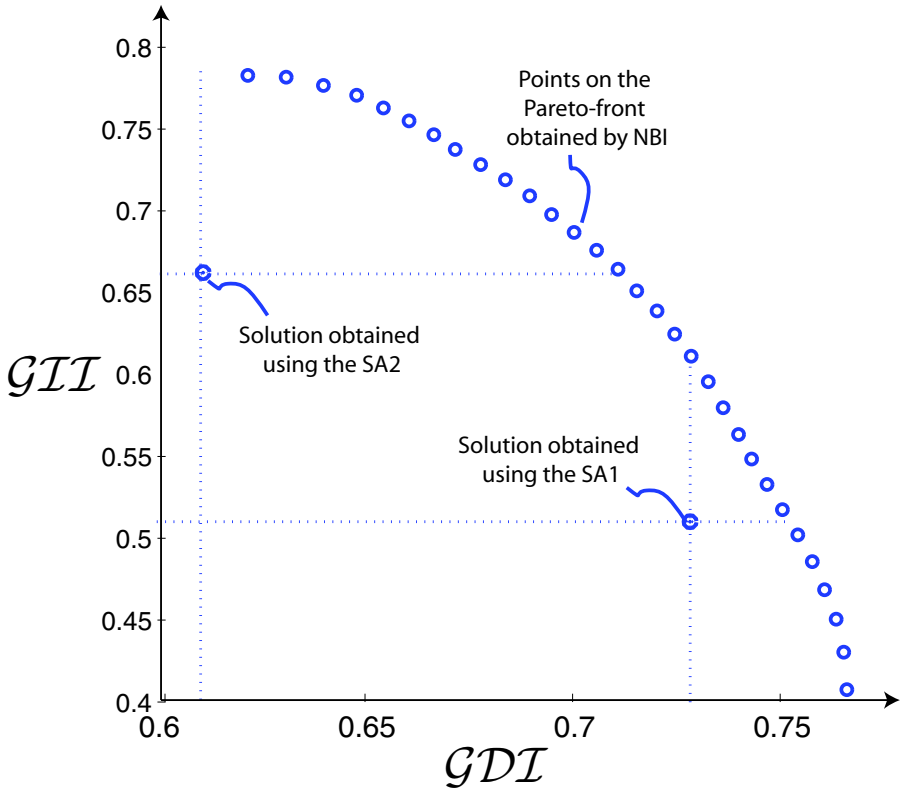

Figure 2.8: Comparison of sequential approach with the Pareto-front curve.

ators, a new lower limit can be imposed on the link lengths as $l_0 > 40$mm, rendering the last 11 points on the Pareto-front curve as infeasible designs. As for the second constraint, the footprint of the mechanism is to be restricted. The designer can impose constraints of different footprint areas to observe their effect on the non-dominated solution set. In Figure 2.10 infeasible solutions for footprint area of 400mm x 400mm are marked. Noticing that there are still many feasible solutions on the current Pareto-front curve, one can calculate the weights of the limit points of the feasible set using the curve fit. The limiting points have weights of $\lambda \approx 0.1$ and $\lambda \approx 0.2$, respectively. A final decision can be done considering the final use of the device in question. In this Chapter, the device is aimed to be used as a high fidelity haptic interface and more emphasis is given on the $\mathcal{GDI}$ value since this metric highly affects the closed loop control performance of the final design. Therefore, the point $\lambda \approx 0.1$, labeled as a star in Figure 2.10, is selected as the final design. The link lengths corresponding to this design choice are also represented in Figure 2.10.

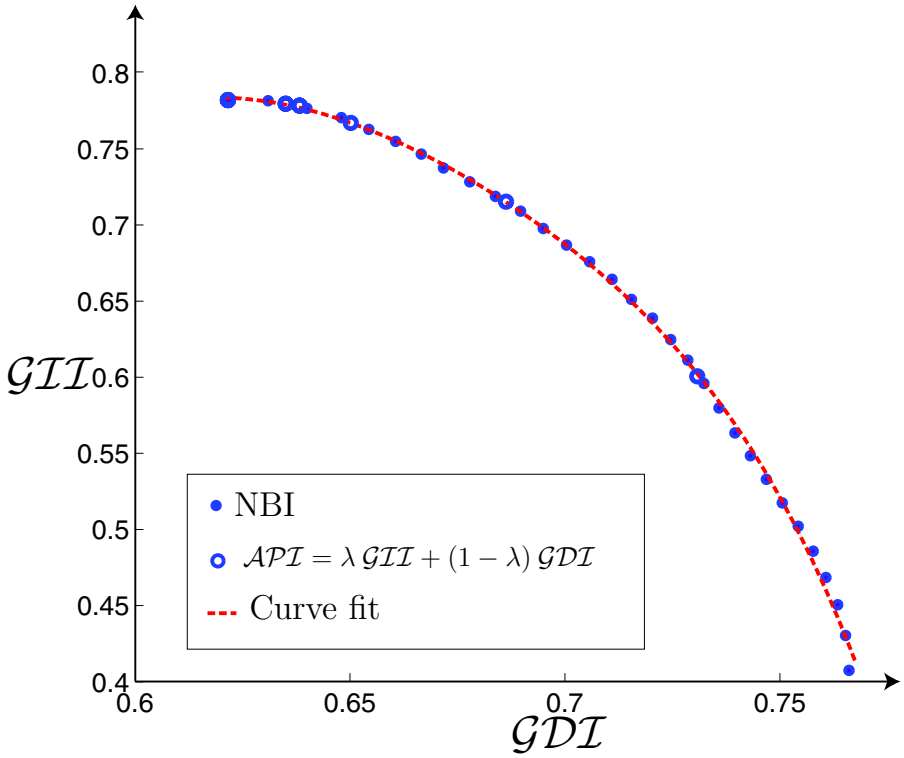

Figure 2.9: Comparison of NBI and aggregated performance index methods. Symbol λ is the weighting factor.

2.6 Conclusions and Future Work

In this Chapter, a general framework suitable for the design optimization of parallel mechanisms with respect to the multiple design criteria is presented. Optimization problems for parallel mechanisms employed as force feedback device with best worst-case kinematic and dynamic performance are formulated. Non-convex single objective optimization problems are solved with the culling algorithm, while NBI method is used to obtain the Pareto-front curve to present the designer with a wide range of alternative solutions. Computational efficiency of NBI method is demonstrated over aggregating approaches such as weighted sums. The optimality of the design using Pareto methods is shown over prioritization approaches. To facilitate the determination of the "best" solution of the Pareto set, estimation of the relative weights of performance indices that are implicit in the Pareto plot is presented. Dimensional synthesis of a high performance parallel robot utilizing the Pareto-front curve is demonstrated.

The method presented can be extensible to work with the other type of per-

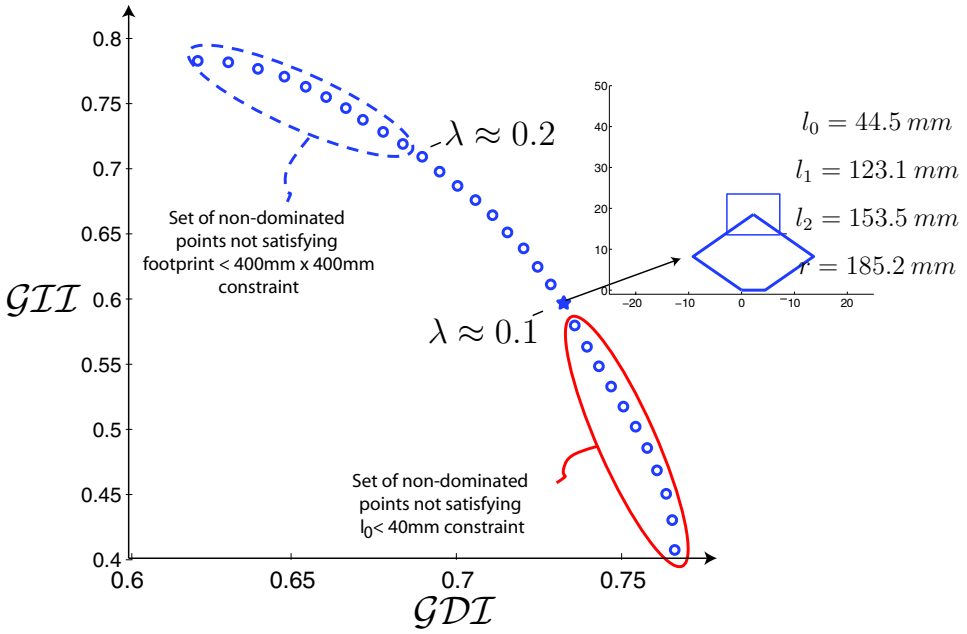

Figure 2.10: Effects of additional constraints imposed on the problem and link lengths and weights corresponding to "best" designs.

formance indices and to include more than two criteria that does not violate the sufficient smoothness of the trade-off surface. Implementation details of NBI method is presented in Appendix B. Application of the proposed framework to the design of more complex parallel mechanisms incorporating increased number of design parameters and objectives will be addressed in the future.

Chapter 3

Optimal Dimensional Synthesis of Force Feedback Lower-Arm Exoskeletons

Force feedback exoskeletons are wearable computer-controlled motorized devices that serve as a haptic interfaces to physically couple human operators with rendered virtual environments. Ideal haptic devices are desired to withstand human applied forces with very high stiffness and be capable of displaying a full range of impedances down to the minimum value humans can perceive. The performance of a haptic interface under closed loop control is measured by the transparency of the display, that is, by quantifying the match between the desired and actually rendered impedance values. During haptic rendering, the haptic interface is coupled to the control system and its existence results in parasitic effects on the displayed impedances, deteriorating the perfect transparency. Low effective inertia is crucial, especially while rendering impedance values at the lower end of the spectrum. Even though inertia cancelation can be implemented in control, issues like sensor and quantization noise limit the applicability of these approaches. A haptic interface with isotropic performance is also of interest, since such a design will result in a more uniform "feel" of the device throughout the workspace, while simultaneously making most efficient use of the available actuators. Therefore, independent of the control algorithm used, both the kinematic and dynamic performance of a haptic device have substantial impact on the overall performance of the haptic display.

Since, most of the requirements for haptic interfaces are satisfied by parallel mechanisms thanks to their inherent characteristics like low inertia, compactness, high stiffness, high position and force bandwidths, and high isotropy, parallel mechanism based lower-arm exoskeletons are discussed in this Chapter. However, di-

mensions of the parallel mechanisms must be fine tuned to achieve the highest performance from such devices as haptic interfaces. In addition, trade-off relations between conflicting performance requirements must be systematically resolved since intuition may fail due to complexity of the analysis of parallel mechanisms. Given a kinematic structure determination of the optimal dimensions of a parallel mechanism to satisfy multiple design criteria is highly challenging task.

Besides the important task of determining the most appropriate dimensions of a given parallel mechanism architecture that constitute the best compromise between multiple performance criteria, another relevant concern during design optimization studies is the selection of the most appropriate kinematic structure [6]. Selection of the most appropriate kinematic structure for a given task is non-trivial, since kinematics and dynamics of each mechanism may differ substantially from each other and intuitive approaches may fail to capture the important trade-offs among multiple mechanisms. Studies that address this design challenge are rare in the literature. Recently, Chablat *et al.* [6] presented a interval analysis based comparison study for three degrees of freedom parallel kinematic structures, in which two parallel mechanisms are compared with respect to their workspace and kinetostatic performance. Similarly, in [25] a comparative study of of parallel mechanisms is conducted with respect to their workspace and stiffness. Finally, in [64] the singularity free workspace and size of parallel mechanisms are compared. Even though these studies compare multiple parallel mechanisms with respect to their performance for a given task, they cease to capture the multi-objective nature of the problem, and do not provide a complete view of the performance trade-offs while selecting one mechanism over other. Based on pareto optimality concepts, this Chapter aims to provide a formal approach for rigorous comparison of multiple mechanisms with respect to multiple design criteria.

In this Chapter, kinematic and dimensional synthesis of lower arm exoskeletons are conducted using the multi-criteria design optimization framework introduced in [60, 61]. The optimized devices are aimed to be employed as a high fidelity haptic interfaces for human forearm and wrist. Multiple design objectives for the devices are discussed and classified for the application scenario at hand, and optimization problems to study the trade-offs between these criteria are formulated. Dimensional

syntheses are performed for optimal global kinematic and dynamic performance of two spherical parallel mechanisms (SPMs) that satisfy the ergonomic necessities of a human forearm and wrist. Then, two mechanisms are rigorously compared with respect to the design criteria based on their pareto optimal solution sets and advantages/disadvantages of each design are discussed. Finally, kinematic structure and dimensions of an optimal exoskeleton are decided in the light of Pareto-front curves generated.

The Chapter is organized as follows: Section 3.1 introduces the kinematic model of human lower arm and discusses the selection two SPMs as the candidate kinematic structures. Section 3.2 summarizes the kinematic and singularity analysis of the two SPMs. Several design objectives appropriate for exoskeleton devices the are identified and categorized in Section 3.3. Section 3.4 formulates the multi-criteria optimization problems, explains the optimization methods used to address them, and presents, and discusses the results of multi-criteria optimization problems. Section 3.5 presents the formal comparison of the two parallel mechanisms and justifies selection of one over the other. Finally, Section 3.6 concludes the Chapter.

3.1 Kinematics of Human Lower-Arm and Spherical Parallel Mechanisms

The movement of human wrist is quite complex since it is capable of lateral flexion and extensions motions around the radiocarpal and midcarpal joints axes as well as abduction and adduction motions about an axis that passes through the capitate. Moreover the whole human wrist is capable of supination and pronation movements about the axis of the forearm. Even though the rotation axes of these motions are subject to small variations as the joints move, simplified kinematics of the human elbow and wrist can be quite faithfully modeled as a three degrees of freedom (DoF) kinematic chain that allows supination/pronation of the forearm and flexion/extension and abduction/adduction of the wrist joint. In the simplified kinematic model, the axes of rotation for these three motions coincide at a single point on the wrist. Workspace and torque limits of human forearm and wrist are listed in Table 3.1.

Table 3.1: Workspace and Torque Limits of Human Forearm and Wrist

Joint	**Human Isometric Strength** [48]	**Human Joint Workspace Limits**
Forearm Supination/Pronation	9.1 Nm	Supination: 86° Pronation: 71°
Wrist Palmar/Dorsal Flexion	19.8 Nm	Palmar Flexion: 73° Dorsiflexion: 71°
Wrist Abduction/Adduction	20.8 Nm	Adduction: 33° Abduction: 19°

A kinematic chain that is suitable to serve as an exoskeleton should have rotation axes of its joints coincident with the rotation axes of human wrist when the device is worn by an operator. Moreover, the choice of closed kinematic chains (parallel mechanisms) are preferable over their serial counterparts in satisfying requirements of force feedback applications, since parallel mechanisms possess inherent advantages. Specifically, parallel mechanisms offer compact designs with high stiffness and have low effective inertia since their actuators can be grounded, or placed on parts of the mechanism that experience low accelerations, in many cases. In terms of dynamic performance, high position and force bandwidths are achievable with parallel mechanisms thanks to their light but stiff structure. Besides, parallel mechanisms do not superimpose position errors at joints, hence can achieve high precision.

In order to span an acceptable portion of the natural human wrist and forearm workspace and to ensure alignment of the axes of rotation of human joints with the controlled DoF of the device such that decoupled actuation and measurement of human joint rotations are possible, two closed kinematic chain based mechanisms, namely 3R$\underline{\text{P}}$S-$\underline{\text{R}}$[1] and 3U$\underline{\text{P}}$S-S mechanisms, are selected as the candidate kinematic structures of the exoskeleton. Both mechanisms belong to the larger family of spherical parallel mechanisms (SPMs). Even though there has been important recent advances in the type synthesis of SPMs [32, 28, 13], design and analysis of many of even the most basic types of these mechanisms are still open research topics [4]. 3R$\underline{\text{P}}$S and 3U$\underline{\text{P}}$S-S mechanisms are among the few SPMs, whose kinematic and sin-

[1]Parallel mechanisms are commonly denoted by using symbols U, R, S, and P, which stand for universal, revolute, spherical, and prismatic joint. Symbols corresponding to actuated joints are underlined in this notation.

gularity analyses are fully addressed in the literature. Moreover, being compact and allowing for human arm motions without collisions with the device, these two mechanisms are the most suitable SPMs to serve as wearable force feedback devices.

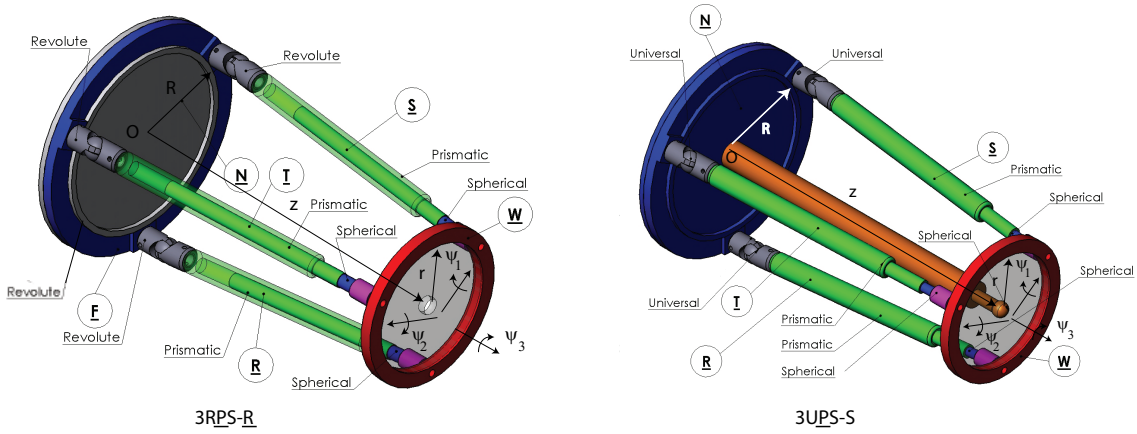

Figure 3.1: 3RPS-R and 3UPS-S mechanisms in perspective views

3RPS-R and 3UPS-S mechanisms are depicted in Figure 3.1. The 3RPS-R mechanism is of hybrid kinematic structure and comprises of a 3RPS parallel wrist in series with an actuated revolute (R) joint at the base platform of the wrist, while the 3UPS-S mechanism is purely parallel and comprises of a 3UPS parallel wrist coupled with the kinematics of the idealized human wrist that acts as a spherical (S) joint at the moving platform of the mechanism.

The 3RPS platform, first introduced by Lee *et al.* [37], and further analyzed in [40], consists of five bodies: a base platform F, three extensible links R, S, T, and a moving platform W. The end-effector held by the operator is rigidly attached to the moving platform W. Extensible links are connected to the base platform via revolute joints whose axes of rotation are oriented along the tangents of F, while the moving platform is connected to the extensible links by means of spherical joints. In this Chapter, the analysis is limited to a symmetric 3RPS mechanism where the revolute joints and the spherical joints are spaced at 120° along the circumference of the base platform of radius R and the moving platform of radius r, respectively.

The 3RPS-R mechanism has four DoF corresponding to the height z and Euler angles ψ_1, ψ_2 and ψ_3 of the moving platform W with respect to the Newtonian reference frame N. The rotation of the base platform and the lengths of the extensible links are actuated to control these DoF. The platform possesses limited translational

movement transverse to the vertical axis through the base and no singularities for limited values of revolute joint angles $q_i \in (0, \pi/2)$ [37]. The 3R$\underline{\text{P}}$S-$\underline{\text{R}}$ mechanism is first utilized as an exoskeleton device by Gupta *et al.* [18] and adapted as a rehabilitation device in [19].

The 3U$\underline{\text{P}}$S-S mechanism, first analyzed in [21], also consists of five bodies: a base platform N, three extensible links R, S, T, and a moving platform W. The end-effector held by the operator is rigidly attached to the moving platform W. The wrist of the operator is idealized as a spherical joint and the forearm of the operator is fixed to the base platform N. Hence, for this mechanism, the human arm counts as a part of the kinematic structure[2]. Extensible links are connected to the base platform via spherical joints, while the rotating platform is connected to the extensible links (and human forearm) by means of spherical joints (and wrist). In this Chapter, the analysis is limited to a symmetric 3U$\underline{\text{P}}$S-S mechanism where the universal joints and the spherical joints are spaced at 120° along the circumference of the base platform of radius R and the moving platform of radius r, respectively. Initial configuration of the 3U$\underline{\text{P}}$S-S mechanism selected as $\psi_1 = \psi_2 = 0$ and $\psi_3 = 90°$ so that the mechanism possesses the best kinematic isotropy at the initial configuration.

The 3U$\underline{\text{P}}$S-S mechanism has three DoF corresponding to Euler angles ψ_1, ψ_2 and ψ_3 of the moving platform W with respect to the Newtonian reference frame N. The lengths of the extensible links are actuated to control these DoF. The moving platform is a distance z from the base platform and does not possess translational movement transverse to the vertical axis through the base. No singularities exist for this mechanism for limited values of revolute joint angles $q_i \in (0, \pi/2)$ [4]. The 3U$\underline{\text{P}}$S-S mechanism is first utilized as an exoskeleton device by Yang *et al.* [66, 67].

Since the performance of parallel mechanisms is highly sensitive to their dimensions, optimization studies are absolutely necessary for design of these types of mechanisms [46]. Moreover, comparison of two kinematic chains can only be performed once they are both optimized for the same set of performance criteria. In this Chapter, optimal dimensions for both of these mechanisms will be calculated

[2]Note that kinematics of human arm is not required to be considered in the analysis of 3R$\underline{\text{P}}$S-$\underline{\text{R}}$ mechanism since unlike the case for 3U$\underline{\text{P}}$S-S, kinematics of human arm only imposes redundant constraints to 3R$\underline{\text{P}}$S-$\underline{\text{R}}$ mechanism.

with respect to multiple design criteria to be detailed in the next sections, and then a rigorous comparison will be conducted between the two mechanisms.

3.2 Kinematic, Dynamic, and Singularity Analyses of 3RPS-R Mechanism

This section summarizes the kinematic, dynamic and singularity analyses performed for the 3RPS-R mechanism, so that kinematic Jacobian J and apparent inertia M matrices can be formulated to be used in the design optimization studies. Similar analyses are also performed for the 3UPS-S mechanism, but these derivations are omitted in text for the sake of briefness.

3.2.1 Kinematic and Singularity Analyses

The aim of this analysis is to summarize the necessary steps for derivation of the configuration level kinematics and the kinematic Jacobian of 3RPS-R and 3UPS-S mechanisms. The kinematic Jacobian matrices of the mechanisms are required by the optimization routines such that their kinematic performance can be characterized. To construct the kinematic Jacobian, the end-effector velocities are to be expressed in terms of the velocities of the actuators through a forward kinematics analysis.

To set the notation, let a symbol in standard typeface represent the length of the corresponding vector marked by an arrow. Let each rigid link of the mechanism be defined as a body and assign a vector basis to each body with the first basis vector extending along the link length.

For 3RPS-R, define bodies F, W, R, S, and T along with their vector bases are shown in Figure 3.2. The end-effector point is denoted by E while the symbol N is used to signify the Newtonian reference frame. Point O represents a fixed point in N, which is selected as the origin. Configuration variables ψ_1, ψ_2, and ψ_3 denote the end-effector orientation with respect to space123 Euler angle set, while x, y, and z denote the end-effector position in the Newtonian frame N. Points F_R, F_S, F_T, and W_R, W_S, W_T locate the revolute joints and spherical joints on bodies

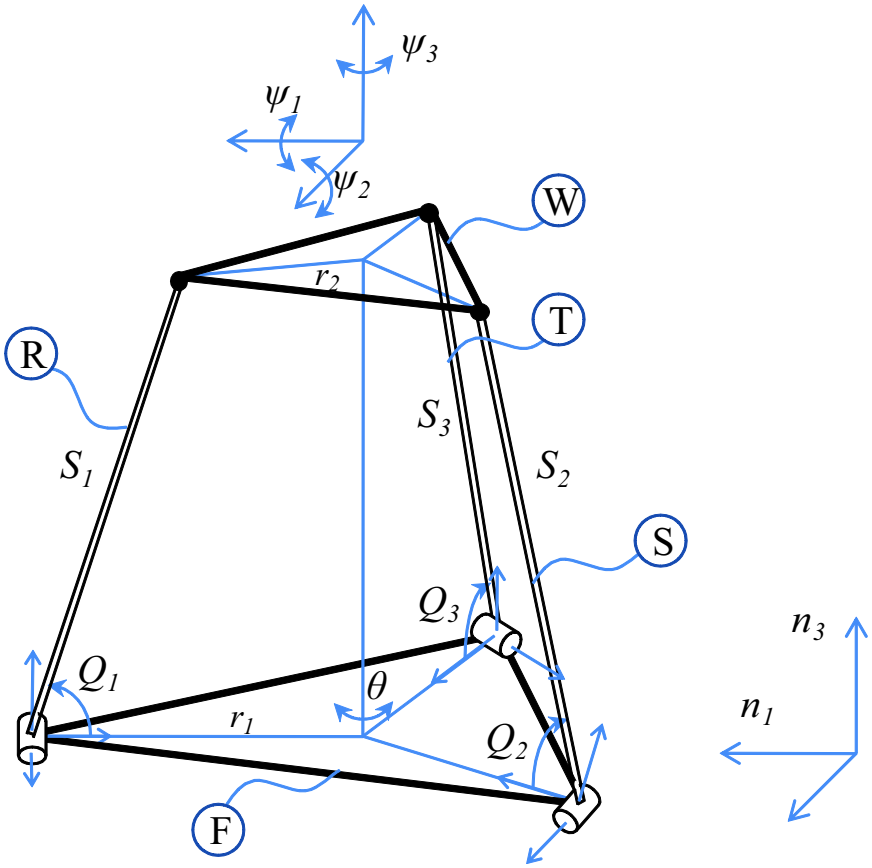

Figure 3.2: Sketch of 3RPS-R Mechanism used in Kinematic and Dynamic Analyses

F and W, respectively. The varying link lengths of prismatic joints, that is, the distances between the points F_R and W_R, F_S and W_S, F_T and W_T, are measured by configuration variables s_1, s_2, s_3. The configuration variable θ is defined to measure the orientation of F with respect to the basis vector $\overrightarrow{n_1}$. Finally, the orientations of the links R, S and T about their revolute joint axes with respect to the body F are given by configuration variables q_1, q_2, and q_3, respectively. The vector loop equations enforcing the closed kinematic chain for the 3RPS-R mechanism can be written as

$$-\rho_1 \overrightarrow{f_{a_1}} + s_1 \overrightarrow{r_1} + \rho_2 \overrightarrow{w_{a_1}} - \overrightarrow{p^{OE}} = \overrightarrow{0} \tag{3.1}$$

$$-\rho_1 \overrightarrow{f_{b_1}} + s_2 \overrightarrow{s_1} + \rho_2 \overrightarrow{w_{b_1}} - \overrightarrow{p^{OE}} = \overrightarrow{0} \tag{3.2}$$

$$-\rho_1 \overrightarrow{f_{c_1}} + s_3 \overrightarrow{t_1} + \rho_2 \overrightarrow{w_{c_1}} - \overrightarrow{p^{OE}} = \overrightarrow{0} \tag{3.3}$$

where, ρ_1 and ρ_2 are the distance between the center of F and axes of the revolute joints and the center of W and the axes of the spherical joints, respectively. The

vector $\overrightarrow{p^{OE}}$ is the position vector from point O to E, and can be written as

$$\overrightarrow{p^{OE}} = x\,\overrightarrow{n_3} + y\,\overrightarrow{n_2} + z\,\overrightarrow{n_3} \tag{3.4}$$

These three vector equations are equivalent to nine nonlinear scalar equations in 13 configuration variables. For the configuration level forward kinematics ψ_1, ψ_2, ψ_3, q_1, q_2, q_3, x, y, z are the unknowns to be solved for, while for the configuration level inverse kinematics s_1, s_2, s_3, θ, q_1, q_2, q_3, x, y are the unknowns. Since no closed form analytical solution is possible for these set of equations, one can solve the configuration level forward/inverse kinematics of the 3RPS-R mechanism utilizing numerical methods, such as the Newton-Raphson method.

Spatial and temporal coherence exist during kinematic and dynamic simulation of mechanisms; hence, once properly initialized local search methods, like Newton-Raphson, continue to converge to the correct solution as long as the simulation step size is selected to be sufficiently small. However, such a coherence need not exist in optimization routines; hence, proper initialization of unknown configuration variables constitutes an important concern during design optimization studies. In this study, global performance indices, that require a full span of the workspace, are utilized; hence, one can take advantage of spatial coherence during initialization given sufficiently fine discretization of the workspace.

Good initial value estimates for s_1, s_2, s_3, θ, q_1, q_2, q_3, x, and y for solution of configuration level inverse kinematics are estimated through a geometric interpretation of vectors. Expressing the vectors connecting the revolute joints to the spherical joints as the function of ψ_1, ψ_2, ψ_3, θ, x, and y as

$$s_1\overrightarrow{r_1} = -(-\rho_1\,\overrightarrow{f_{a_1}} + \rho_2\,\overrightarrow{w_{a_1}} - \overrightarrow{p^{OE}}) \tag{3.5}$$

$$s_2\,\overrightarrow{s_1} = -(-\rho_1\,\overrightarrow{f_{b_1}} + \rho_2\,\overrightarrow{w_{b_1}} - \overrightarrow{p^{OE}}) \tag{3.6}$$

$$s_3\,\overrightarrow{t_1} = -(-\rho_1\,\overrightarrow{f_{c_1}} + \rho_2\,\overrightarrow{w_{c_1}} - \overrightarrow{p^{OE}}) \tag{3.7}$$

one can estimate the link lengths s_1, s_2, and s_3 assuming that $x = y = 0$ and $\theta = 0$ for the starting configuration, when $\psi_1 = \psi_2 = \psi_3 = 0$. Initial values of q_1, q_2, and q_3 can be estimated by evaluating the angle between the prismatic joints and F under the same assumptions.

Defining motion variables u_1, u_2, and u_3 such that the angular velocity of W with respect to N is represented as ${}^N\overrightarrow{\omega}^F = u_1\,\overrightarrow{n_1} + u_2\,\overrightarrow{n_3} + u_3\,\overrightarrow{n_3}$ and evaluating the

time rate of change of vector loop equations (3.1)–(3.3) in the Newtonian reference frame, one can formulate the motion level equations for the motion variables u_1, u_2, u_3 and the time derivatives of dependent configuration variables $\dot{q}_1$, $\dot{q}_2$, $\dot{q}_3$, $\dot{x}$, $\dot{y}$, $\dot{z}$ in terms of the linear speeds of the prismatic actuators $\dot{s}_1$, $\dot{s}_2$, $\dot{s}_3$ and angular velocity of the forearm actuator $\dot{\theta}$ as

$$A\ [u_1\ u_2\ u_3\ \dot{z}\ \dot{q}_1\ \dot{q}_2\ \dot{q}_3\ \dot{x}\ \dot{y}]^T = B\ \left[\dot{s}_1\ \dot{s}_2\ \dot{s}_3\ \dot{\theta}\right]^T \tag{3.8}$$

Then, the velocity level forward kinematics of the 3RPS-R mechanism, characterizing the relationship between end-effector and actuator velocities, can then be obtained by extracting the Jacobian matrix (J) as

$$\begin{bmatrix} u_1 \\ u_2 \\ u_3 \\ \dot{z} \end{bmatrix} = J \begin{bmatrix} \dot{s}_1 \\ \dot{s}_2 \\ \dot{s}_3 \\ \dot{\theta} \end{bmatrix} \tag{3.9}$$

Unlike mechanisms with serial kinematic chains, parallel mechanisms may possess kinematic singularities within their workspace. Such singularities are undesirable and their elimination is aimed during the design phase. In this study, singularities of the 3RPS-R mechanism are checked exhaustively by imposing constraints on the condition numbers of the A and B matrices such that they are not ill-conditioned.

Finally, physical and kinematic constraints $\zeta_i < 90^\circ$ and $q_i < 90^\circ$ (i = 1, 2, 3) are imposed to the design optimization problem during calculation of the performance indices. Here, ζ_i 's represent the variations of the angles between prismatic link and wrist plate, and constraint on ζ_i's are imposed to ensure a design with workspace limits that satisfies the range of motion limits of commercially available spherical joints. The second kinematic constraint ensures the positive displacement pose of the mechanism.

3.2.2 Formulating the Apparent Inertia Matrix

To formulate the apparent inertia matrix D of the system as seen at the end-effector, dynamic analysis is performed employing Kane's method. In Kane's method, one carries out dot products between partial velocity vectors and applied and inertia

forces, and between partial angular velocity vectors and applied and inertia torques. The partial velocity and partial angular velocity vectors are obtained by inspection of the pertinent velocity and angular velocity expressions, identifying coefficients of the corresponding generalized speeds [24, 15]. Then, a summation of terms over all particles and bodies in the 3RPS-R mechanism produces expressions for the generalized active force F_r $(r = 1, \ldots, 13)$ and the generalized inertia force F_r^* $(r = 1, \ldots, 13)$. The dynamical differential equations are then contained in $F_r + F_r^* = 0$ $(r = 1, \ldots, 13)$, which may be arranged as

$$M(\xi)\dot{\tilde{\mathbf{u}}} = \boldsymbol{\Upsilon}(\boldsymbol{\xi}, \tilde{\mathbf{u}}, t). \tag{3.10}$$

where M is the inertia matrix of the mechanism in terms of independent generalized speeds $\tilde{\mathbf{u}} = [u_1\ u_2\ u_3\ \dot{z}]$. The effective inertia matrix D of the system as seen at the end-effector can then be calculated from M according to the formula

$$D = J^{-T} M J^{-1}. \tag{3.11}$$

3.3 Design Objectives

Following the terminology of Merlet [46], one can categorize the performance requirements of a mechanism into four distinct groups: *Imperative* requirements that must be satisfied for any design solution, *optimal* requirements for which a maximal value of the index is required, *primary* requirements which take place in the specifications but can be modified to some extend to ensure a design solution, and *secondary* requirements which do not appear in the specifications but can be utilized to choose between multiple design solutions.

Ensuring the safety and complying with the ergonomic needs of the human operator are two imperative design requirements every exoskeleton device must satisfy. Safety is typically assured by recruitment of back-drivable impedance type devices[3] with force/torque limits implemented in software, while the ergonomy of the device

[3]Our discussion is limited to impedance type devices due to their widespread use as haptic exoskeletons, even though admittance type devices might possibly be used with inclusion of appropriate safety equipment.

is considered at the kinematic synthesis level. Predetermined workspace volumes are imposed for the application and being capable of spanning all of the desired workspace and ensuring alignment of the axes of rotation of human joints with the controlled DoF of the device, both 3RPS-R and 3UPS-S mechanisms satisfy the ergonomic requirements of a lower arm exoskeleton. The absence of singularities in the workspace is another imperative design requirement the both mechanisms satisfy, that ensures the forward and inverse kinematics of the robots can be solved uniquely at each point within the workspace.

The performance requirements to be optimized are highly dependent on the final use of the device. For a high fidelity haptic interface, kinematic/dynamic isotropy and stiffness of the device (including the actuator and transmission compliance) should be maximized while effective moving mass should be minimized to achieve high force bandwidths and a uniform "feel" for the device.

Optimal performance of mechanisms are quantified through study of several design matrices, including kinematic Jacobian (J) and inertia matrix (M). In this Chapter global performance measures, characterizing the performance of a manipulator over the entire workspace are considered.

To quantify the kinematic/dynamic performance of the haptic interface global isotropy index ($\mathcal{GII}$) and global dynamic index ($\mathcal{GDI}$) are proposed in [57]. Both of these indices are conservative workspace inclusive worst-case performance measures that are intolerant of poor performance over the entire workspace. An optimal $\mathcal{GII}$ results in a uniform kinematic Jacobian matrix, while optimizing $\mathcal{GDI}$ minimizes the effective inertia matrix of the system. Other commonly used global isotropy indices include average (AII) and standard deviation ($SDII$) of the local isotropy index over the workspace. Since the stiffness of both system are dominated by the compliance of the transmission and actuators, optimization for a Jacobian matrix with high (AII) will result in maximization of the stiffness of the device.

Since entries of kinematic Jacobian and inertia matrices of the 3RPS-R mechanism are not homogenous in units, scaling factors need to be introduced for this mechanism. Scaling factors eliminate the physical units and normalize the elements of these matrices as fractions of their maximum values so that comparable relative values are ensured [57].

As mentioned in Section 3.1, the 3RPS-R mechanism is of hybrid kinematic structure, that is, it is composed of both parallel and serial kinematic chains, while the 3UPS-S is a purely parallel mechanism. To allow for a fair comparison between the two mechanisms according to their kinematic and dynamic performances, scaling for 3RPS-R is performed with placing special attention to its series characteristic. Note that inputs from the actuator placed at the series revolute joint of 3RPS-R mechanism map to the end effector rotations (ψ_3) with unity gain, while the actuated prismatic joints can map the remaining end effector rotations (ψ_1 and ψ_2) with much less gain due to the parallel kinematic structure. Global kinematic isotropy requires these mappings to stay uniform and close over the workspace. Realizing that rotary actuators with different power output characteristics than the actuators at the prismatic joints can be employed at this revolute joint, scaling due to asymmetric power outputs of the actuators can be performed to ensure best isotropy of the overall device.

A scaling constant, hence power output characteristic of the rotary actuator with respect to linear drives, is selected such that the best-worst kinematic performance ($\mathcal{GII}$) of 3RPS-R is determined by the 3RPS parallel platform of part the device. A proper scaling constant is selected from Figure 3.3 by plotting the minimum of the minimum singular values and maximum of the maximum singular values in the workspace of the two rows of the Jacobian matrix related to ψ_1 and ψ_2 over the parameter space. In this Chapter, the scaling constant is selected as 0.02 such that the singular value introduced due to the rotary actuator is never one of the extreme values of the eigenvalues; hence, the serial kinematics of 3RPS-R has no effect on calculation of $\mathcal{GII}$.

The primary requirement for the wearable exoskeleton is selected as the workspace volume index [46], the ratio between the workspace volume and the volume of the robot. Even though predetermined workspace volume is imposed as an imperative requirement, a large workspace volume index is desirable to reduce the collisions of the device with the operator and the environment. The weight of the device is highly dependent on the selection of the actuators, more so than the link lengths; hence, there exists some flexibility on deciding the total mass of the kinematic structure.

Finally, the secondary requirements for both devices include low backlash, low-

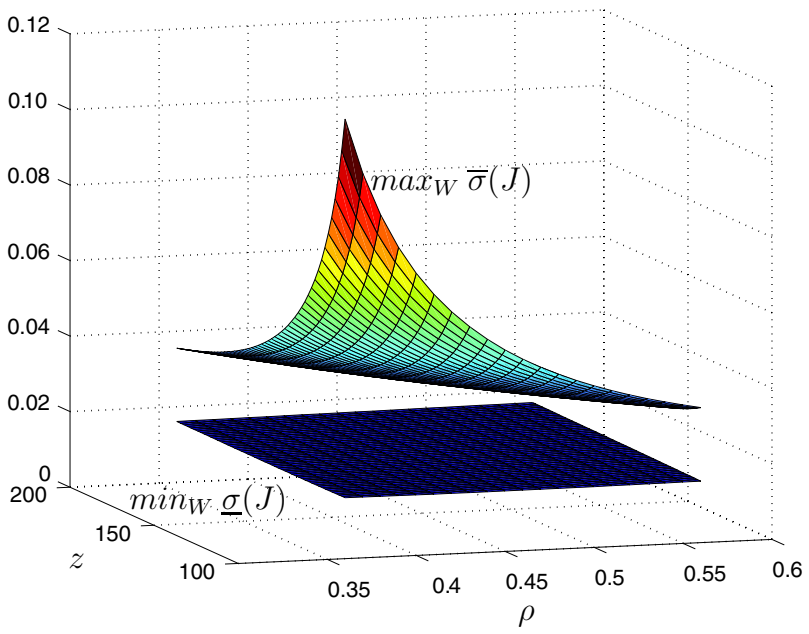

Figure 3.3: Minimum of minimum and maximum of maximum singular values of J over the parameter space

friction, high back-drivability, and low manufacturing costs. Friction, backlash and back-drivability are mainly influenced by the selection of the actuators and the transmission, while choice of link lengths may have an influence on manufacturing costs.

3.4 Optimization of Spherical Parallel Mechanisms

3.4.1 Multi-criteria Optimization Problem

For optimal dimensioning of the exoskeleton as a high fidelity haptic interface, two objective functions characterizing the kinematic and dynamic performance of the mechanism are considered. The objective of optimization is to maximize the worst kinematic isotropy of the mechanism ($\mathcal{GII}$) while simultaneously minimizing the effective inertia (max singular value of the effective inertia matrix or $\mathcal{GDI}$).

The negative null form of the multi-objective optimization problem can be stated

as

$$\begin{aligned} max\ \ & \mathbf{F}(\boldsymbol{\alpha}, \boldsymbol{\beta}, \boldsymbol{\gamma}) \\ & \mathbf{G}(\boldsymbol{\alpha}, \boldsymbol{\beta}) \leq 0 \\ & \mathbf{H}(\boldsymbol{\alpha}, \boldsymbol{\beta}) = 0 \\ & \boldsymbol{\alpha}_l < \boldsymbol{\alpha} < \boldsymbol{\alpha}_u \end{aligned} \tag{3.12}$$

where $\mathbf{F}$ represents the column matrix of objective functions that depend on the design variables $\boldsymbol{\alpha}$, parameters $\boldsymbol{\beta}$, and workspace positions $\boldsymbol{\gamma}$. Symbol $\mathbf{G}$ and $\mathbf{H}$ represents the inequality and equality constraint functions that also depend on design variables and parameters. Finally, $\boldsymbol{\alpha}_l$ and $\boldsymbol{\alpha}_u$ correspond to the lower and upper bounds of the design variables, respectively.

The symmetric 3R$\underline{\text{P}}$S-$\underline{\text{R}}$ and 3U$\underline{\text{P}}$S-S mechanisms both have two parameters $\beta_1 = r$ and $\beta_2 = W$, where r is the radius of the moving platform and selected according to statistical data on human joint sizes listed in [19] and $W = \psi_1 \times \psi_2 \times \psi_3$ represents the predetermined workspace. The workspace is set as $W = 30° \times 30° \times 60°$ for the design of the high fidelity haptic interface. The optimization problem has two design variables: the ratio of the moving and base platform radii $\alpha_1 = r/R$ and the perpendicular distance of the moving platform $\alpha_2 = z$. Upper $\boldsymbol{\alpha_u}$ and lower $\boldsymbol{\alpha_l}$ limits on the design parameters are imposed according to statistical data on human arm [19].

The column matrix of objective functions for the haptic interface $\mathbf{F}$ is given as

$$\mathbf{F} = [\, GII \quad GDI \,]^T \tag{3.13}$$

while inequality and equality constraints $\mathbf{G}$ and $\mathbf{H}$ are imposed during kinematic analysis to ensure the closed kinematic chain for the 3R$\underline{\text{P}}$S and 3U$\underline{\text{P}}$S-S platforms and the positive perpendicular travel pose of the mechanisms, respectively.

3.4.2 Solution Methods

The multi-criteria design optimizations of the 3R$\underline{\text{P}}$S-$\underline{\text{R}}$ and 3U$\underline{\text{P}}$S-S parallel mechanisms are conducted using the framework introduced in [60, 61]. This optimization framework for parallel mechanisms is based on NBI method [11] to efficiently obtain the Pareto-front hyper-surfaces characterizing the design trade-offs. Based on gradient techniques, the approach is more efficient than other methods to obtain

a well represented Pareto-front hyper-surface including aggregate methods such as weighted sums and evolutionary optimization approaches such as GAs.

3.4.3 Results

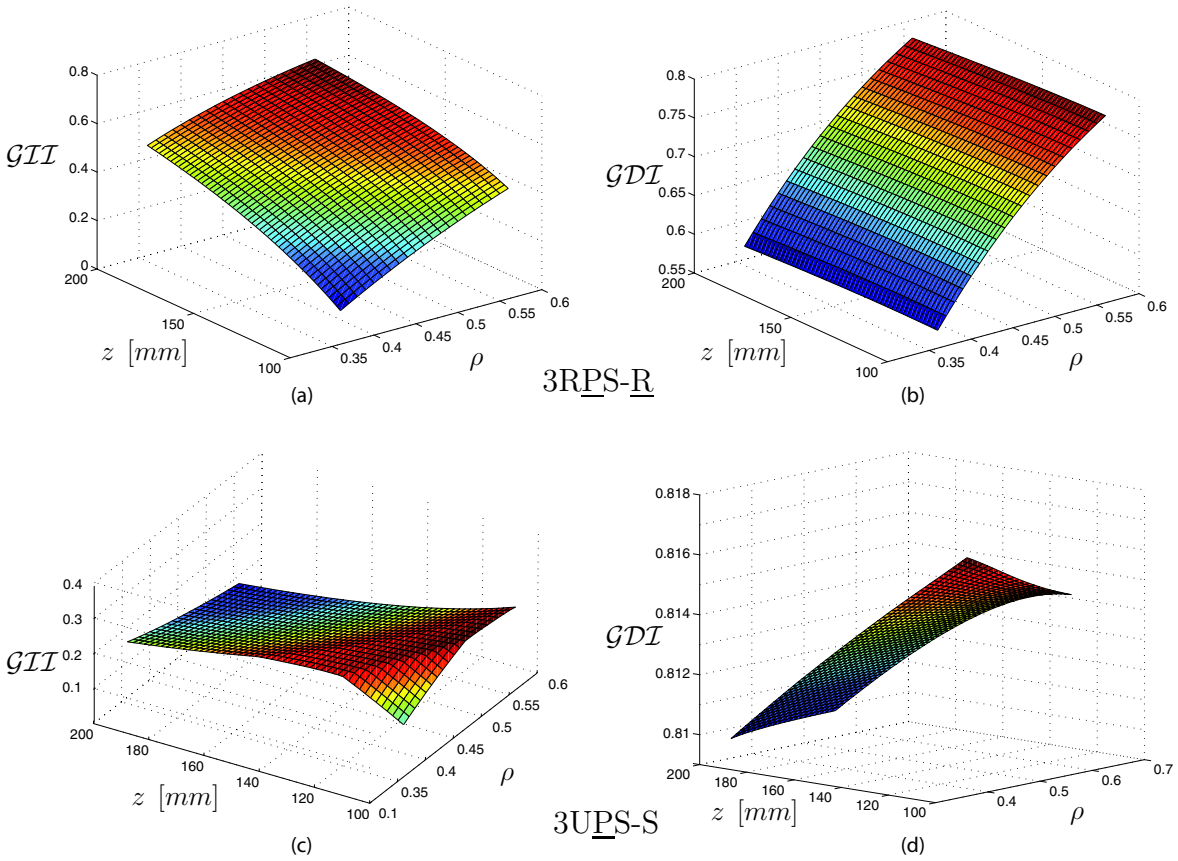

Figure 3.4: Change of $\mathcal{GII}$ and $\mathcal{GDI}$ for 3RPS-R and 3UPS-S mechanisms over parameter space

Figure 3.4(a) and (b) present the distribution of $\mathcal{GII}$ and $\mathcal{GDI}$ of 3RPS-R device over the parameter space. Similarly, Figure 3.4(c) and (d) present the distribution of $\mathcal{GII}$ and $\mathcal{GDI}$ of 3UPS-S device over the parameter space. From these plots one can observe that both $\mathcal{GII}$ and $\mathcal{GDI}$ indices vary an important amount for different parameter values of the 3RPS-R mechanism, while the variance is much less for the 3UPS-S mechanism.

In fact, dynamic isotropy ($\mathcal{GDI}$) of the 3UPS-S device is almost uniform over the parameter space, effects of parameter changes being minimal. The situation is quite different for the 3RPS-R mechanism and such behavior is expected since the

3RPS platform part of this device rotates around the fixed base, causing the change in link lengths have an important effect on the effective inertia. In Figure 3.4(d) the variation of $\mathcal{GDI}$ for the 3UPS-S device is negligible, while such variation is about 10 times higher for the 3RPS-R device in Figure 3.4(b).

Kinematic isotropy ($\mathcal{GII}$) of the 3RPS-R mechanism also varies substantially as the parameters are changed. Moreover, the 3RPS-R device can achieve much larger $\mathcal{GII}$ values than the 3UPS-S device. The variation of kinematic isotropy of the 3UPS-S mechanism under different parameter values is important and the characteristic of this change is complex.

To characterize the trade-off between the single objective solution of each mechanism, Pareto-front curves for the bi-objective optimization problem is constructed in Figures 3.5 and 3.6 employing the NBI method. Figure 3.5 presents uniformly distributed points on the Pareto-front curve characterizing the trade-off between $\mathcal{GII}$ and $\mathcal{GDI}$ for the 3RPS-R device, while Figure 3.6 depicts the same plot for the 3UPS-S device. Since the $\mathcal{GDI}$ values changes only a negligible amount for the 3UPS-S, the Pareto-front curve for this device is effectively a straight line along which only the parameter ρ changes from 0.36 to 0.47 almost monotonically while the perpendicular platform distance $z = 100\,mm$. The Pareto-front of the 3RPS-R device is convex curve along which values of optimal parameters varies from $\rho = 0.56$, $z = 100\,mm$ to $\rho = 0.36$, $z = 200\,mm$ in a non-trivial manner.

Singularity analysis are performed for the Pareto optimal sets of each mechanism, and largest singularity free portion of the human lower-arm workspace each design can span are determined and labeled on the Figures.

3.5 Comparison, Selection of an Optimal Mechanism, and Discussion

To allow for comparison of the multi-criteria performance of both mechanisms, their Pareto-front curves are presented on the same plot in Figure 3.7. From this plot one can conclude that 3UPS-S mechanism possesses a much better dynamic performance than all mechanisms that are possible with the 3RPS-R kinematic structure. However, further analysis of the maximum singular values of M for both mechanisms

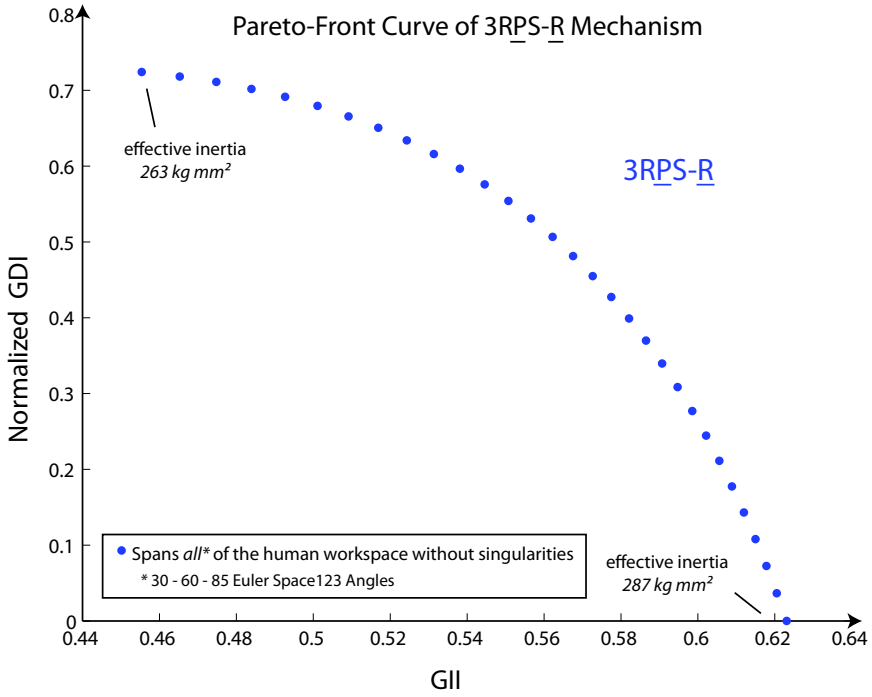

Figure 3.5: Pareto-front curve for 3RPS-R mechanism

reveals that effective inertia of the 3RPS-R mechanisms are not so much higher than the effective inertia 3UPS-S devices, assuming identical links are used during their construction. On the other hand, best worst case kinematic performance ($\mathcal{GII}$) of the 3RPS-R mechanisms are about two times better than kinematic performances of all possible 3UPS-S devices. Moreover, all of the 3RPS-R mechanisms in the Pareto-front set can span the entire workspace of human lower-arm in a singularity-free manner, while 3UPS-S mechanisms in the Pareto-front set can do so for only a portion of the human workspace.

Placing an higher emphasis on the kinematic performance and considering the primary objective of workspace volume index the optimal kinematic structure is selected as the 3RPS-R kinematic structure.

Since the performances of different non-dominated solution solutions on the Pareto-front curve of 3RPS-R mechanism spans a considerable range, it is up to the designer to choose the "best" design for the application at hand. This decision is challenging since the relative weights of performance criteria are not transplant, but implicit in the Pareto plot. Luckily, for the convex portions of the Pareto-front curve, it is always possible to estimate the relative weight λ of the objective functions since there exists an explicit relationship between the slope of the Pareto curve

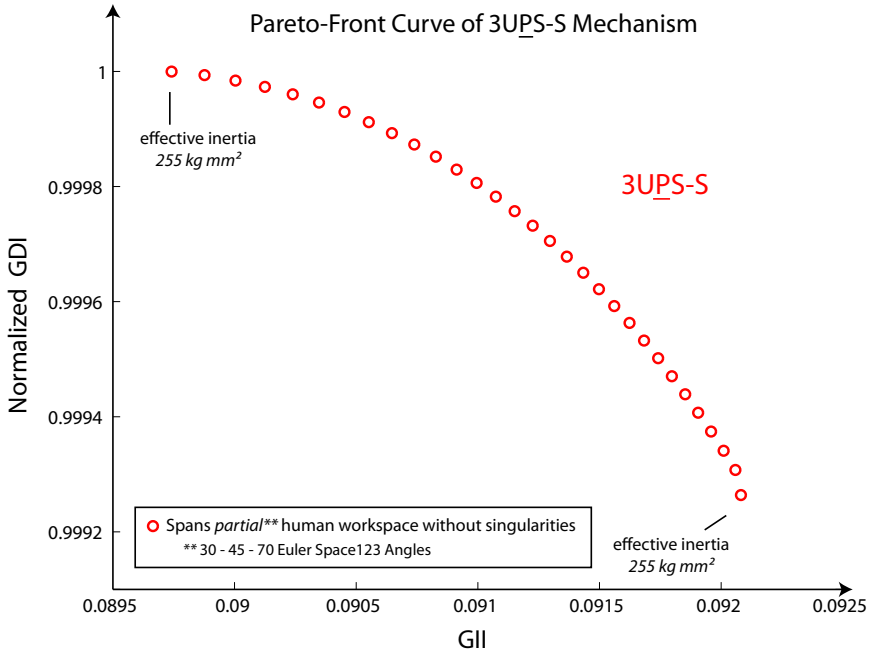

Figure 3.6: Pareto-front curve for 3UPS-S mechanism

at a Pareto point and λ [10]. Reflecting the relative importance (preference) among the objective functions under consideration, weights help negotiating the decision trade-offs within the Pareto set.

To estimate the weights of points on the Pareto set, a polynomial of 5^{th} order is fitted with $R^2 = 0.99999974$ on the points obtained using NBI method as shown in Figure 3.7. Given the slope (θ) of this curve at any point, relative weight λ of the objective functions can be estimated as $\lambda = 1/(1-\theta)$. To select a design, thresholds of 0.5 are imposed on the Pareto-front curve of 3RPS-R mechanism, one for each performance criteria, rendering only a limited number of points in the Pareto-front set feasible. The limiting points on the feasible set are estimated to have weights of $\lambda \approx 0.6$ and $\lambda \approx 0.8$, respectively. To choose a design that lies halfway in between the limiting points, a final decision is done by selecting the non-dominated design with $\lambda \approx 0.7$, labeled as a star in Figure 3.7. The parameter values of the optimal design are $\rho = 0.47$ and $z = 191$mm.

3.6 Conclusions

Multi-criteria design optimization of a parallel mechanism based force-feedback exoskeleton for human forearm and wrist is presented. Relevant design objectives for

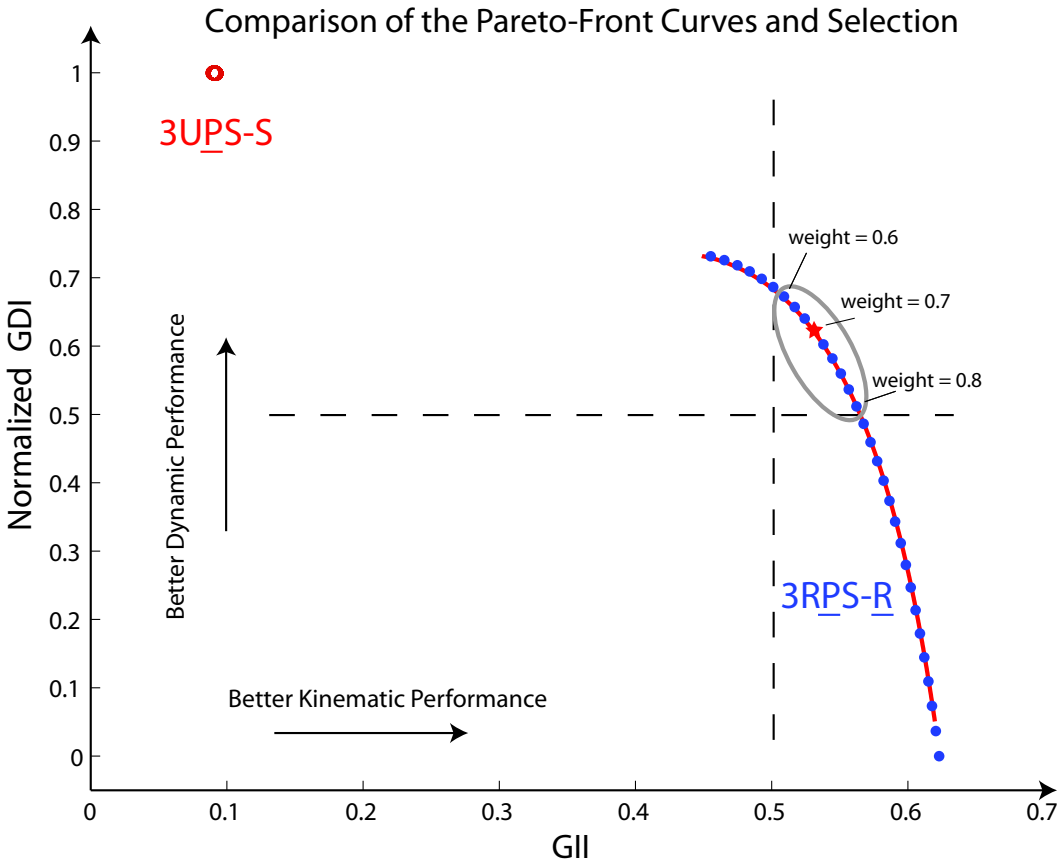

Figure 3.7: Comparison of Pareto-front curves for 3RPS-R and 3UPS-S mechanisms for $\mathcal{GII}$ vs $\mathcal{GDI}$

force-feedback exoskeleton devices are identified and categorized. Rigorous comparison of two spherical parallel mechanisms that satisfy the ergonomic necessities of a human forearm and wrist is presented, by extending a Pareto front based multi-criteria optimization framework developed for parallel mechanisms and the kinematic structure that results in superior performance for force-feedback applications is selected. Optimal dimensional synthesis of a spherical parallel mechanism based lower arm exoskeleton is conducted to ensure an optimal trade-off between global kinematic and dynamic performance of the device.

Chapter 4

Modeling and Control of a Lower-Arm Exoskeleton

From Hardiman to Sarcos' exoskeleton, many design studies on exoskeleton devices have been presented in the literature; however, this challenging topic is still open for research due to the complex trade-offs among ergonomy, safety, and performance requirements of these devices. In 1960's and 1970's initial studies on exoskeleton systems were held for teleoperation applications to facilitate manipulation in hazardous environments. The first man-amplifying exoskeleton system, "Hardiman", was comprised of a small master exoskeleton placed in a large slave exoskeleton, which is actuated hydraulically. Hardiman was designed for lifting/carrying and had 30 degrees of freedom. Instability due to hydraulic sensors, danger of leakage from hydraulic circuit, and heavy weight were the main design bottlenecks of this design [47]. Salisbury/JPL arm [3] was developed in early 1980's and employed in bilateral teleoperation tasks as a force reflecting master device. A thorough discussion of early stages and recent studies of the exoskeleton systems can be found in [5] and [18].

Early exoskeleton systems were task oriented and had drawbacks regarding to performance and ergonomic constraints. The state of the art exoskeleton systems like BLEEX, HAL, and SARCOS have already addressed many of these challenges, thanks to the rapid progress in actuation, computation, and controls technologies. For the arm exoskeleton systems, successful implementation of force feedback applications were first realized in [44], workspace constraints were studied in [52] and a more ergonomic design was presented in [9]. These studies tackled the the performance and ergonomic constraints by changing actuation system from pneumatic to electrical in [70] or by using pneumatic muscle actuators in [48].

Most of the existing arm exoskeleton devices are of serial kinematic structure. On the other hand, it is well established that parallel mechanisms can satisfy high-fidelity haptic interface requirements, due to their inherent advantages such as high stiffness, high position/force bandwidths with respect to their serial counterparts. However, modeling of parallel mechanisms is more challenging and more importantly these devices possess smaller workspace with possible singularities within this workspace, rendering satisfaction of the ergonomic constraints a challenging task. In the literature, parallel mechanism based arm exoskeleton systems are proposed in [23, 66] and [18].

In [65], a 7 DoF (4-RPS-1R-3RPS) full arm exoskeleton is proposed. This device can satisfy ergonomic constraints, while also approaching to the standards of a high-fidelity haptic display. In this design, pneumatic actuators are preferred for the actuation to provide smooth motion that is compatible with the human arm. Design parameters of the mechanism are selected by assigning weights to the indices related ergonomy and performance of the haptic display. In [66], Yang *et al.* developed a lightweight and cost-effective 7 DoF parallel mechanism based exoskeleton system. The mechanism consists of a 3 DoF spherical joint for the shoulder, 1 DoF revolute joint for the elbow and a 3 DoF spherical joint for the wrist. Since there exists a functional analogy between the human muscles and the cable based transmission, in this design each joint are driven by cables arranged in parallel. As a result, the system is lightweight, possesses high dexterity and large workspace [67]. Finally, Gupta *et al.* , presented a hybrid (parallel + serial) mechanism based exoskeleton, RiceExo, which has been exploited for rehabilitation and training [18]. The RiceExo can cover 90% of the human forearm workspace and makes use of direct drive to avoid compliance, nonlinearities, and backlash associated with transmissions.

Even though many conflicting design criteria need to be taken into account during design of an exoskeleton, many of these studies only consider a single (or aggregate) objective function to conduct optimization studies. A formal multi-criteria design optimization study for exoskeleton devices has recently been conducted in [63] and a rigorous comparison of devices introduced in [66] and [18] is undertaken. In this study, the better kinematic structure is decided and the optimal dimensional synthesis of this mechanisms is completed according to multiple design criteria suit-

able for force feedback exoskeleton interfaces.

This Chapter is organized as follows: Section 4.1 presents the kinematic and dynamic analyses of the lower arm exoskeleton. Design and hardware components of the device are detailed in Section 4.2. Section 4.3 briefly summarizes the implementations of the model based task-space position and impedance controllers and presents simulation results.

4.1 Dynamical System Modeling Analysis

Kinematic and dynamic analyses of the lower arm exoskeleton system to be uses for the real-time implementation of the controllers are presented in this section. Before going into details of analyses brief introduction of Kane's method is presented.

There exist several methods to formulate equations of motion for constrained multi-body systems. Even though the solutions of the resulting equations are the same, form of the equations sets and the numerical solution methods required to solve these equations depend on the formulation method.

In this study, Kane's method is selected to formulate equation of motion of the exoskeleton system due to two major features of this method that can lead to efficient formulation of the system dynamics. In Kane's method, non-working forces can be neglected at the beginning of the analysis by eliminating them through use of vector algebra. Since these forces have no contributions to the final solution, this elimination results in equations that are in more compact form. Moreover, through effective use of generalize coordinates and *generalized speeds*, the equations of motion can be represented using a minimal set of variables. As a result, Kane's equations may lead to more compact and efficient representation of system kinematic and dynamic models, that are suitable for real-time implementations.

4.1.1 Formulating Kinematical and Dynamical Differential Equations

The configuration of the 3RPS-R mechanism is described by 13 generalized coordinates ξ_r $(r = 1, \ldots, 13)$. To enable the formulation of compact and efficient equations of motion [54], define 13 generalized speeds u_r $(r = 1, \ldots, 13)$ as linear

combinations of the generalized coordinate derivatives $\dot{\xi}_r$ $(r = 1, \ldots, n)$ [26]. Express these definitions using

$$\mathbf{u} = \boldsymbol{K}\dot{\boldsymbol{\xi}} + \boldsymbol{L}, \tag{4.1}$$

where $\mathbf{u}$ and $\dot{\boldsymbol{\xi}}$ are 13×1 matrices of u_r and $\dot{\xi}_r$, and where the elements of the 13×13 matrix K and 13×1 matrix L are functions of ξ_r $(r = 1, \ldots, 13)$. The matrices K and L are chosen such that the angular velocity of W with respect to N is represented as ${}^N\overrightarrow{\omega}^F = u_1\,\overrightarrow{n_1} + u_2\,\overrightarrow{n_2} + u_3\,\overrightarrow{n_3}$, and $u_m = \dot{\xi}_m$ $(m = 4, \ldots, 13)$, where $\boldsymbol{\xi} = [\psi_1\ \psi_2\ \psi_3\ z\ q_1\ q_2\ q_3\ x\ y\ s_1\ s_2\ s_3\ \theta]^T$. Note that the reciprocal relations also exist in which the generalized coordinate derivatives are expressed in terms of the generalized speeds:

$$\dot{\boldsymbol{\xi}} = \boldsymbol{V}\mathbf{u} + \boldsymbol{\varepsilon}, \tag{4.2}$$

where the elements of the 13×13 matrix V and 13×1 matrix ε are functions of ξ_r $(r = 1, \ldots, 13)$. Equation (4.2) is the matrix representation of the kinematical differential equations, and forms the first of two portions of the state equations or equations of motion that govern the behavior of the mechanism.

The second portion, the dynamical differential equations, will be expressed in explicit form as

$$\dot{\mathbf{u}} = \boldsymbol{\Upsilon}(\boldsymbol{\xi}, \mathbf{u}, t) \tag{4.3}$$

which is derived using Kane's method. Such a representation is possible since no configurations of the system exist for which the motion of one or more bodies is not resisted by inertia. In Kane's method, one carries out dot products between partial velocity vectors and applied and inertia forces, and between partial angular velocity vectors and applied and inertia torques. The partial velocity and partial angular velocity vectors are obtained by inspection of the pertinent velocity and angular velocity expressions, identifying coefficients of the corresponding generalized speeds. Then, a summation of terms over all particles and bodies in the 3RPS-R mechanism produces expressions for the generalized active force F_r $(r = 1, \ldots, 13)$ and the generalized inertia force F_r^* $(r = 1, \ldots, 13)$. The dynamical differential equations

are then contained in $F_r + F_r^* = 0$ $(r = 1, \ldots, 13)$, which may be arranged as in Eqn. (4.3).

4.1.2 Handling the Constraint Equations

The 3RPS-R mechanism is subject to 9 configuration (holonomic) constraints given as

$$\boldsymbol{\Gamma}(\boldsymbol{\xi}) = 0. \tag{4.4}$$

In this study, the configuration constraints are imposed within the solver utilizing Newton-Raphson iterations at each time step[1]. The configuration constraints are also differentiated to produce constraint equations that are linear in the motion coordinates, yielding

$$\boldsymbol{B}\mathbf{u} + \boldsymbol{C} = 0, \tag{4.5}$$

where the elements of the 9×13 matrix B and the 9×1 matrix C are functions of ξ_r $(r = 1, \ldots, 13)$. These constraints are then used to undertake a local coordinate transformation to eliminate dependent motion variables from the equations [26]. This process projects the dynamical differential equations onto the 4-dimensional constraint manifold, in which the solution of (4.3) is constrained to lie [39, 16]. In this study, the projection is carried out using symbolic operations (realizing a dot product) in contrast to numerical operations and is called *embedding* the constraints.

To embed the constraints in Kane's method, express the 9 dependent generalized speeds in terms of the remaining 4 independent generalized speeds by carrying out linear operations on the constraint equations (4.5). Re-order and partition the generalized speeds in (4.5) to produce:

[1] An alternative to imposing the configuration constraints within the solver, that is performing Newton iterations on Eq. (4.4) at each time step, is to calculate the configuration by integrating the motion constraints. However, in this approach numerical or initialization errors in the motion constraints will lead to violations of the configuration constraints –violations that can accumulate and slow down the integration over long simulations. Since the initialization and round-off errors at the motion (velocity) level will remain relatively constant during integration [24], the violation to the configuration constraints will only grow linearly with time. There exist simple stabilization techniques to overcome this problem [54].

$$B_1 \begin{bmatrix} u_5 \\ \vdots \\ u_{12} \end{bmatrix} = B_2 \begin{bmatrix} u_1 \\ \vdots \\ u_4 \end{bmatrix} + C. \tag{4.6}$$

where u_r $(r = 1, \ldots, 4)$ are the independent generalized speeds and u_r $(r = 5, \ldots, 13)$ are the dependent generalized speeds. Now that the motion constraints have been expressed in an explicit linear form, the derivation of the constrained dynamical differential equations proceed by eliminating the dependent generalized speeds from the analysis and applying Kane's method as usual. The equations of motion in the independent generalized speeds are then simply formed as:

$$\tilde{F}_r + \tilde{F}_r^* = 0 \quad (r = 1, \ldots, 4) \tag{4.7}$$

which are only 4 ordinary differential equations in the 4 unknowns, u_r $(r = 1, \ldots, 4)$. Finally, equations (4.7) may be used to produce explicit equations for $\dot{u}_r$ in the form

$$\dot{\tilde{\mathbf{u}}} = \tilde{\boldsymbol{\Upsilon}}(\boldsymbol{\xi}, \tilde{\mathbf{u}}, t) \tag{4.8}$$

where $\tilde{\mathbf{u}}$ is a 4×1 matrix of the independent generalized speeds.

The resulting dynamic differential equations are a set of ordinary differential equations, and yield to solution with a standard ODE solver. Advantages associated with embedding constraints include the reduction in the number of equations to be integrated and robustness due to the disappearance of the instability problem associated with the integration of differentiated constraints in DAE solvers.

The process outlined above for obtaining equations of motion is aided by the use of symbolic manipulation software. One such symbolic package is Autolev [55] [27] and another is SymSim, a toolbox for MATLAB® created in [15].

4.2 Hardware

CAD model of the 3RPS-R parallel mechanism based exoskeleton is presented in Figure 4.1. For the hardware implementation of the prismatic joints, direct drive linear electric actuators (Copley STA 1104) are preferred to avoid transmission compliances and to satisfy high bandwidth, low friction, and no backlash requirements of

the device. Since direct drive of forearm disc deteriorates the dynamic performance of the device due to additional inertia associated with such an actuators with reasonable torque output, a capstan mechanism driven by a brushed DC motor (Maxon RE-65) is selected. Capstan drive is preferred since this transmission mechanism is backlash and friction free. Dynamic simulations of the device are performed so that actuators that can withstand a reasonable percentage of human joint torques can be identified. Spherical rolling joint (Hephaist SRJ004C) is selected for implementation of the spherical joints, since these components have high stiffness, low friction, high precision, good repeatability, and large workspace range.

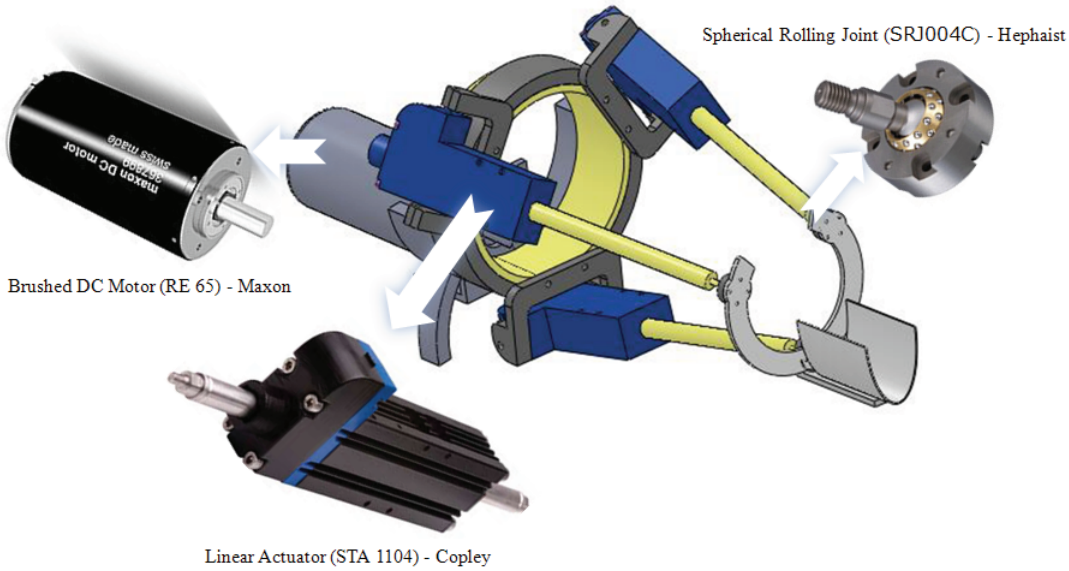

Figure 4.1: CAD Model and Hardware Components of the Lower-arm Exoskeleton Prototype

The direct drive linear actuators have built-in position sensing capabilities, while the DC motor is instrumented with an optical encoder. To drive the motors, linear current amplifiers whose bandwidths are at least an order of magnitude higher than the actuator bandwidth (10 kHz) are selected so that dynamics of the electronic components do not have a significant effect on the system performance.

Figure 4.2 depicts the control hardware designed for the experiments. Since the exoskeleton system is grounded, a workstation based controller architecture is employed. The drivers and sensors are interfaced with the control workstation

through use of an I/O card (Quanser Q8). Host-target architecture is employed for the controller. A multi-core windows PC is utilized as the host as well as the target. Ardence RTX, a hard real-time operation system, is run in the target processor. One of the cores of the CPU is dedicated to the RTX processes all the time for real-time control implementations. Thanks to this dedicated core real-time controllers are realizable at kHz rates. Graphics and high-level controls run at the host side under the Matlab/Simulink environment.

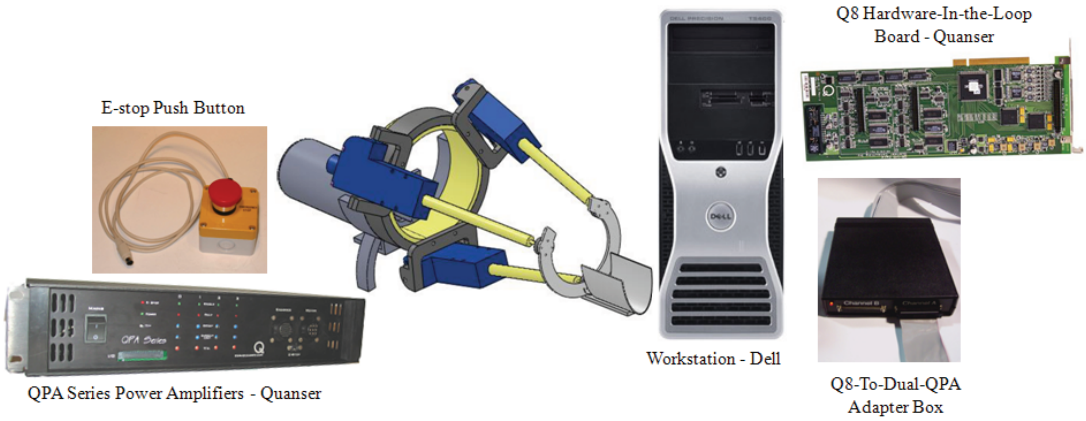

Figure 4.2: Hardware Setup for Real-time Control Implementation of the Lower-arm Exoskeleton

4.3 Control

The main goal of the force feedback exoskeleton device is to a provide haptic interface to physically couple a human operator to virtual environments. Haptic devices are programmed to display the desired stiffness, viscosity, and mass properties of an environment by controlling their actuators. Quality of these interfaces are measured by (i) the accuracy of the impedance displayed (transparency), which is important for high force output applications, and (ii) the impedance resolution (fidelity), which is important for dexterous procedures. Accuracy defines the match between the displayed impedance and the desired impedance and this property is mostly deteriorated by the dynamics of the haptic device. Resolution defines the detection level of impedance discrimination of the haptic interface and dynamics of the haptic devices also deteriorate this property. To cancel out the parasitic effects due to the dynamics of the haptic device, model-based feed-forward compensation

is commonly used.

There are three known criteria for the design of haptic interfaces:

- Free space must feel free; interference due to the device dynamics must be minimum; therefore, the controlled device must have low mass and friction. This requirement is about fidelity and can be achieved by passive design or active control.

- Solid virtual objects must feel stiff; when contact with solid object occur, the controlled haptic device must display an impedance that is as stiff as real solid object. This requirement can be achieved by design of stiff mechanisms and employment of high bandwidth controllers.

- Virtual constraints must not be easily saturated; capability of force production of the haptic mechanism must be high enough to feel solid virtual object. This requirement can be achieved by the fast computation of the control law or selection of powerful actuators.

Force reflection is commonly implemented using one of the two control schemes:

- Impedance control: when the operator dictates the motion, system detects this motion and controls the force applied by the haptic device.

- Admittance control: when the operator dictates the forces applied, the system detects these forces and velocity or displacement is controlled by the system. The type of the haptic controller to be employed is input of the human operator (force/position).

In this section, implementation of computed torque and impedance controllers are presented and the performance of these controllers are presented through simulation results. Admittance control is not implemented since the exoskeleton is not instrumented with force-sensors; however, computed torque control ensures robust trajectory tracking of the device and can serve as the inner position control loop for the admittance controller.

4.3.1 Controller Architectures

Computed Torque Controller

In this part, a brief description of the computed torque method and its implementation are presented.

By rearranging and collecting terms, the equations of motion for the 3RPS-R manipulator in the independent generalized speeds can be expressed as:

$$M(\boldsymbol{\xi})\dot{\mathbf{u}} + C(\boldsymbol{\xi}, \mathbf{u}) + G(\boldsymbol{\xi}) = \boldsymbol{\tau} \tag{4.9}$$

where M is the inertia matrix, C is the Coriolis matrix, and G contains the gravity terms that affect the system. The symbol $\boldsymbol{\tau}$ represents the control torque.

In computed torque control, dynamics of the system should follow the desired values for $\boldsymbol{\xi_d}$, $\dot{\boldsymbol{\xi}}_{\boldsymbol{d}}$, and $\ddot{\boldsymbol{\xi}}_{\boldsymbol{d}}$ taken from a trajectory generator.

The idea behind the computed torque control method is to supply a model based feed-forward torque that cancels the nonlinear terms in the equations of motion, and in addition to that, supply a feedback torque that will ensure robust tracking of the desired trajectory. The control torque for implementation of computed torque method can be calculated as

$$\tau = M(\boldsymbol{\xi})Y(\boldsymbol{\xi})\left[\dot{\boldsymbol{\xi}}_{\boldsymbol{d}} - K_v(W(\boldsymbol{\xi})\mathbf{u} - \dot{\boldsymbol{\xi}}_{\boldsymbol{d}}) - K_p\mathbf{e})\right] + M(\boldsymbol{\xi})\dot{Y}(\boldsymbol{\xi})W(\boldsymbol{\xi})\mathbf{u} + C(\boldsymbol{\xi}, \mathbf{u}) + G(\boldsymbol{\xi}) \tag{4.10}$$

where the tracking error $\mathbf{e}$ is defined as

$$\mathbf{e} = \boldsymbol{\xi} - \boldsymbol{\xi}_d. \tag{4.11}$$

After the application of this control torque, the dynamics of the tracking error can be shown to be

$$M(\boldsymbol{\xi})Y(\boldsymbol{\xi})(\ddot{\mathbf{e}} + K_v\dot{\mathbf{e}} + K_p\mathbf{e}) = 0. \tag{4.12}$$

Since the inertia matrix M is always positive definite for rigid manipulators, and the transformation matrix Y must be selected to be of full rank during dynamic

modeling, the tracking error for the closed loop system will asymptotically converge to zero if K_v and K_p matrices are selected to be positive definite.

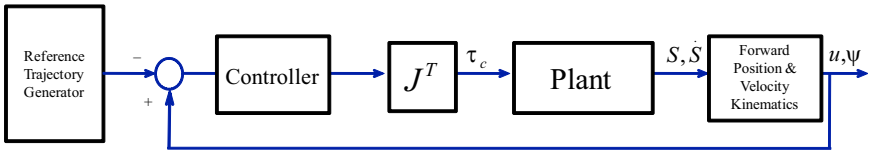

Figure 4.3: Block Diagram of Computed Torque Control

Block diagram of the computed torque control approach is given in Figure 4.3. Simulations of this control scheme are performed in MATLAB/Simulink and C S-functions are written for its real-time implementation.

In Figure 4.4, a reference trajectory for the sinusoidal change in z position of the end-effector with an amplitude of 10 mm at 5 rad/sec is tested, while in Figure 4.5 a reference trajectory for the sinusoidal change in ψ_1 orientation of the end-effector with an amplitude of 0.5 rad at 5 rad/sec is tested to demonstrate that the closed loop system successful tracks these test trajectories.

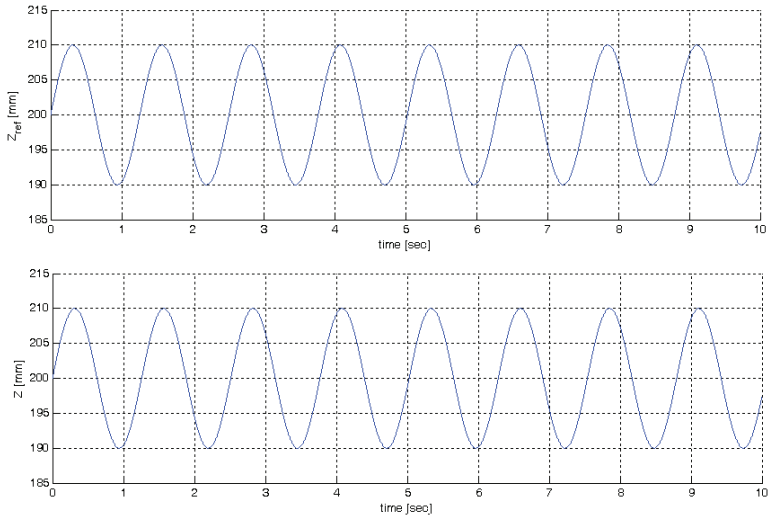

Figure 4.4: Reference trajectory of z and tracking performance of the system

Task Space Impedance Controller without Force Feedback

The block diagram of task space impedance control without force feedback is presented in Figure 4.6 for the linearized device dynamics. Notice that this control architecture is open-loop in the sense that the error in the displayed impedance is

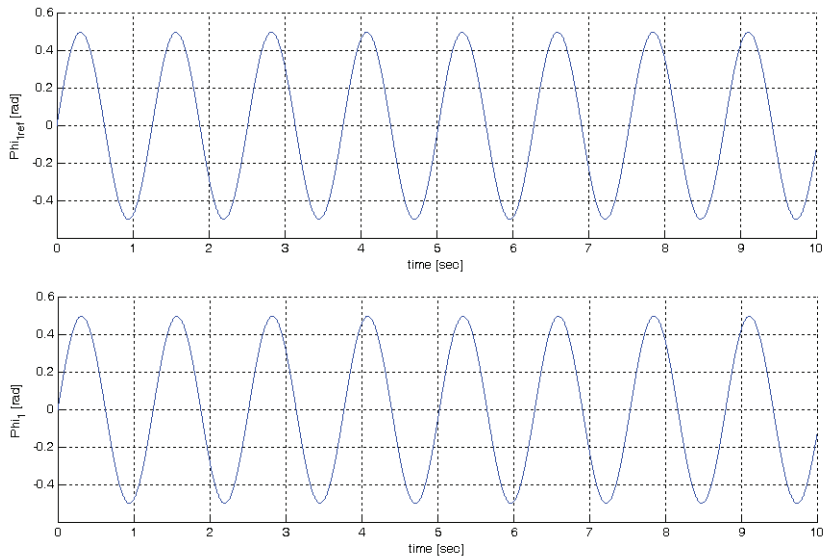

Figure 4.5: Reference trajectory of ψ_1 and tracking performance of the system

not compensated for using sensor measurements since no force feedback is available to measure this impedance.

In the block diagram, after the difference between desired position deflection ($\Delta x_d = x_d - x_o$) and actual position deflection ($\Delta x = x - x_o$) is obtained, this difference and its time derivatives are multiplied with the parameters characterizing the desired impedance to obtain the force values to be reflected at the end effector. The torque commands to the actuators are obtained using the Jacobian matrix. Forces F are the physical inputs which are applied to the system by the human operator.

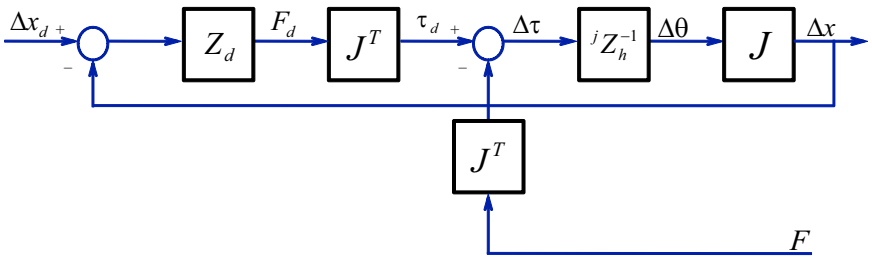

Figure 4.6: Block Diagram of Impedance Controller without Force Feedback

Impedance of the overall control system (Z_C) can be expressed as $-F/\Delta x$ where F is the force applied by the human operator and Δx is the actual position deflection;

$$\Delta x = \left[(\Delta x_d - \Delta x) Z_d J^T - J^T F\right] Z_h^{-1} J \tag{4.13}$$

Defining the linearized impedance of the haptic device dynamics as Z_h and noting that ${}^{j}Z_h = J^{-T}{}^{j}Z_h J^{-1}$, one can obtain

$$Z_h \Delta x = Z_d(\Delta x_d - \Delta x) - F. \tag{4.14}$$

Setting $\Delta x_d = 0$, the impedance of the overall control system can be shown to be equal to,

$$Z_C = Z_d + Z_h \tag{4.15}$$

where Z_d represents the desired impedance. Therefore, the close-loop impedance of the system is equal to the sum of the desired impedance and physical impedance of the haptic device. It can be concluded that, dynamics of the mechanism is a parasitic effect against obtaining the desired impedance in this control architecture.

Task Space Impedance Controller with Feed-forward Dynamics Cancelation and without Force Feedback

Since the perfect transparency cannot be achieved using task space impedance controller without force feedback (open-loop impedance controller) due to the dynamics of the haptic device, model feed-forward can used to compensate for the detrimental effects of device dynamics. If the model of the haptic device is perfectly known, close-loop impedance can be made equal to the desired impedance. Therefore, the more precise information about the model is added, the better control can be achieved. In other words, the torque absorbed by the haptic device $\Delta\tau_{fwd}$ should be added to the system to provide the required torque for the display of desired impedance. Block diagram of open-loop impedance controller with model feed-forward is presented in Figure 4.7.

The torque absorbed by the haptic device, $\Delta\tau_{fwd}$ can be written as

$$\Delta\tau_{fwd} = {}^{j}\hat{Z}_h J^{-1} \Delta x \tag{4.16}$$

where, ${}^{j}\hat{Z}_h$ represents the impedance of the estimated model, and Z_h represents the physical impedance of the haptic device. Δx can be expressed as

$$\Delta x = J^{j}\hat{Z}_h^{-1}[\Delta\tau_{fwd} + J^T F_d - J^T F] \tag{4.17}$$

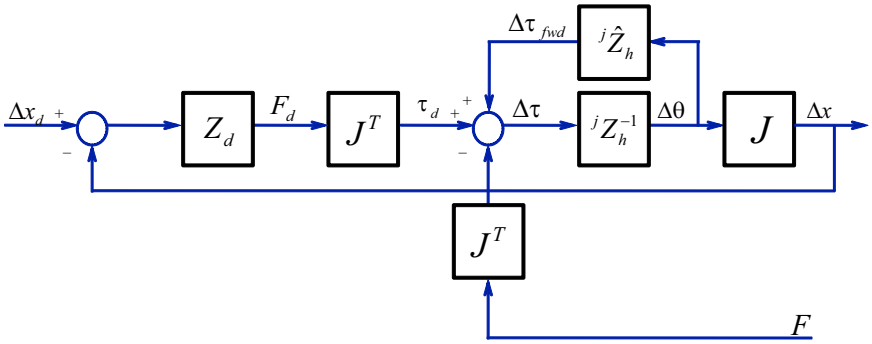

Figure 4.7: Block Diagram of Open-loop Impedance Controller with Model Feedforward

where, F_d is the desired force, which is equal to $Z_d(\Delta x_d - \Delta x)$.

Now, after feedforward compensation impedance of the overall control system can be shown to be equal to

$$Z_C = Z_d + Z_h - \hat{Z}_h. \tag{4.18}$$

While this method can improve the performance as long as the model is close to actual values, its implementation increases the computational time. Thus, feedforward may deteriorate the haptic design stiffness criteria.

Simulations of this control scheme are performed in MATLAB/Simulink and CS-functions are written for the real-time implementation. Simulation results are given in Figures 4.8 and 4.9.

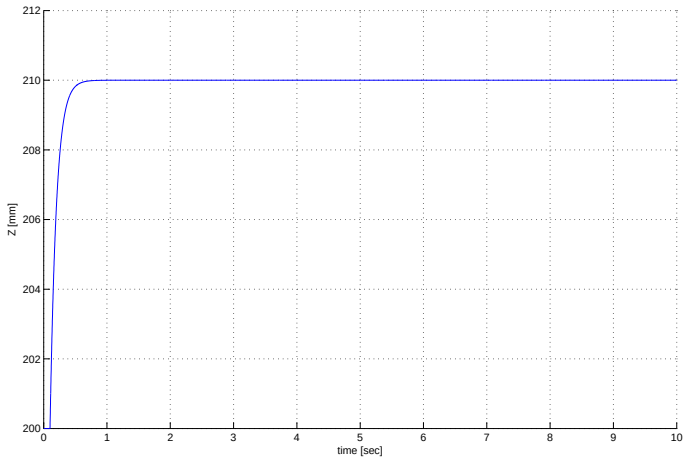

Figure 4.8: z Position of the End Effector Under a Constant Force Excitation

In Figure 4.8, a 10 N force in z direction is exerted on the system after 0.1 seconds. The end-effector position is expected to increase by 10 mm according to impedance gains: the spring coefficient is set to 1 N/mm while the damping coefficient is set to 0.1 Ns/mm. Similarly, in Figure 4.9 a 0.5 Nrad torque is applied about the first axis of end-effector after 0.1 seconds and the end-effector orientation is expected to increase to 0.5 rad according to impedance gains: the spring constant is set to 1 N/rad and the damping coefficient is set to 0.1 Ns/rad. The system behaves as expected for both simulations.

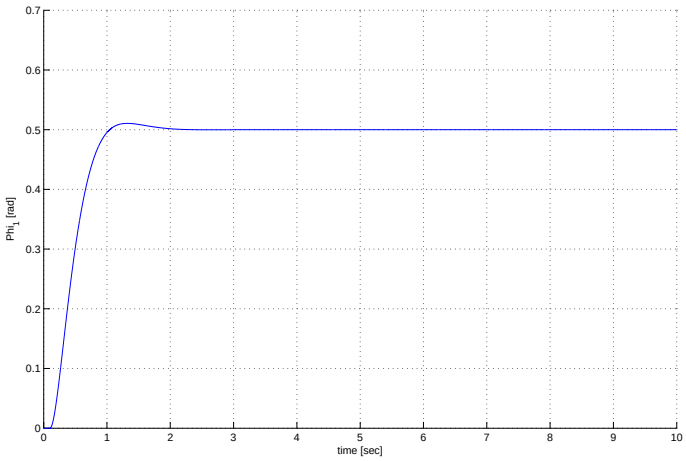

Figure 4.9: ψ_1 Orientation of the End Effector Under a Constant Torque Excitation

Chapter 5

Conclusions and Future Work

In this thesis, we addressed the design, control, and prototyping of an lower-arm exoskeleton to be employed as force feedback device. A general framework for the design optimization of parallel mechanisms has been developed. The framework is extended to allow rigorous comparison of multiple mechanisms. Design optimization has been implemented for spherical parallel mechanisms using this framework and superior kinematic structure and optimum dimensions of the selected kinematic structure are determined to satisfy requirements of a high-fidelity impedance display device. A prototype has been developed, kinematic and dynamic analyses of the design have been conducted. Finally, CS-functions for real-time implementation of position and impedance controllers are prepared and simulations of these controllers are performed.

5.1 Contributions

This thesis comprises of three core chapters that constitute parts of the design procedure of a parallel mechanism based lower-arm exoskeleton.

Chapter II introduces a general framework for design optimization of parallel mechanisms with respect to multiple criteria. The contributions of Chapter II can be listed as follows:

- Kinematic and dynamic performance criteria are reviewed and formulated for sample mechanism,

- Non-convex single-objective optimization problems are solved with a branch-and-bound type (culling) algorithm,

- Normal Boundary Intersection (NBI) method is applied to efficiently obtain the Pareto-front curve for the sample mechanism,

- For design optimization of parallel mechanisms, computational efficiency of NBI method is demonstrated over aggregating approaches, such as the weighted sum method,

- The optimality of the design obtained using Pareto methods is demonstrated over the designs obtained through prioritization approaches,

- Generality (extensibility to work with any set of performance indices and to include any number of criteria) of the proposed framework is discussed.

Chapter III extends the design optimization framework to allow rigorous comparison of multiple mechanisms and presents design optimization of a lower-arm exoskeleton. The contributions of Chapter III can be listed as follows:

- Design objectives for developing force feedback exoskeleton devices are identified and classified,

- Kinematic and dynamic analyses of two spherical parallel mechanism based lower-arm exoskeletons are performed,

- Multi-criteria design optimizations for both mechanism are undertaken with respect to optimal requirements,

- A rigorous comparison of two parallel kinematic structures is presented and optimal dimensional synthesis of a lower-arm exoskeleton is achieved by proper mechanism selection from the Pareto optimal set.

Chapter IV presents the design, dynamic modeling, prototyping, simulation results of position and impedance controllers of a four degree-of-freedom forearm and wrist exoskeleton robot. The contributions of Chapter IV are as follows:

- Prototype of a parallel mechanism based lower-arm exoskeleton is presented,

- Dynamic simulations of the design are conducted to guide motor selection,

- Hardware selection and instrumentation to ensure safety and performance are presented,

- Configuration and motion level (forward and inverse) kinematics of the device are prepared for real-time implementation,

- Computationally efficient solution of (inverse and forward) dynamics of the device is derived using Kane's method,

- Model based task-space position controllers as well as task-space impedance controllers are implemented in simulations.

5.2 Future Directions

Future directions include further study of the design proposed in Chapter IV. Two stage distributed actuation can be implemented to allow for higher bandwidths, while also achieving higher force outputs. Extension can be implemented to accommodate elbow and shoulder motions, such that a full-arm exoskeleton is realized. After the safety of the device is tested, human subject experiments can be carried out to model human arm impedances. Finally, the mechanism can be employed in bimanual and bilateral force feedback applications, such as robot assisted rehabilitation and manual skill training.

Appendix A

Kinematic and Dynamic Analyses of the Five Bar Mechanism

The aim of this appendix is to present the necessary steps for derivation of the kinematic Jacobian and mass matrices of a symmetric five-bar mechanism. To set the notation, let a symbol in standard typeface represent the length of the corresponding vector marked by an arrow.

The kinematic Jacobian matrix of the mechanism is required to determine its kinematics performance. To construct the kinematic Jacobian, the end-effector velocities are to be expressed in terms of the angular velocities of the actuators through a forward kinematics analysis. Let each rigid link of the mechanism be defined as a body and assign a vector basis to each body with the first basis vector extending along the link length. Bodies A, B, C, and D along with their vector bases are shown in Figure A.1. The end-effector point is denoted by E while symbol N is used to signify the Newtonian reference frame. Point O represents a fixed point in N, which is selected as the origin.

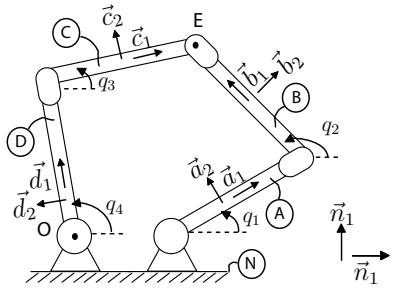

Figure A.1: Symmetric five-bar mechanism with the variables used in the kinematic and dynamic analyses.

Symbols x and y denote the end-effector coordinates in the Newtonian frame N, while the distance between actuators and the link lengths are called l_0 and l_i ($i = 1..4$), respectively. Finally, the orientation of the links are measured with

respect to the basis vector $\vec{n}_1$ and are called q_i $(i = 1..4)$. Note that the mechanism is assumed to be symmetric; hence, the equalities $l_2 = l_3$, $l_1 = l_4$ are in effect.

The vector loop equation enforcing the closed kinematic chain for the symmetric five bar mechanism can be formulated as

$$l_1\vec{a}_1 + l_2\vec{b}_1 - l_2\vec{c}_1 - l_1\vec{d}_1 - l_0\vec{n}_1 = \vec{0}. \tag{A.0.1}$$

Taking time derivative of Eqn. (A.0.1) in the Newtonian frame, one can solve for the time derivatives of dependent variables q_2 and q_3, in terms of the angular speeds of the actuators $\dot{q}_1$ and $\dot{q}_4$ as

$$\begin{bmatrix} \dot{q}_2 \\ \dot{q}_3 \end{bmatrix} = A \begin{bmatrix} \dot{q}_1 \\ \dot{q}_4 \end{bmatrix} \tag{A.0.2}$$

where $A = \begin{bmatrix} \frac{-l_1\sin(q_1-q_3)}{l_2\sin(q_2-q_3)} & \frac{-l_1\sin(q_3-q_4)}{l_2\sin(q_2-q_3)} \\ \frac{-l_1\sin(q_1-q_2)}{l_2\sin(q_2-q_3)} & \frac{-l_1\sin(q_2-q_4)}{l_2\sin(q_2-q_3)} \end{bmatrix}$.

The position of the end-effector E with respect to the fixed point O can be expressed as

$$\vec{p}^{\,OE} = l_1\vec{a}_1 + l_2\vec{a}_2 \tag{A.0.3}$$

while the same position vector can also be expressed in the Newtonian frame as

$$\vec{p}^{\,OE} = x\vec{n}_1 + y\vec{n}_2. \tag{A.0.4}$$

Equating Eqn. (A.0.3) to Eqn. (A.0.4), taking their time derivative in the Newtonian frame, and substituting in Eqn. (A.0.2), one can solve for the velocity level forward kinematics of the five-bar mechanism as

$$\begin{bmatrix} \dot{x} \\ \dot{y} \end{bmatrix} = J \begin{bmatrix} \dot{q}_1 \\ \dot{q}_4 \end{bmatrix} \tag{A.0.5}$$

where the Jacobian matrix

$J = \begin{bmatrix} \frac{-l_1\sin(q_1)-\sin(q_2)\sin(q_1-q_3)}{\sin(q_2-q_3)} & \frac{l_1\sin(q_2)\sin(q_3-q_4)}{\sin(q_2-q_3)} \\ \frac{l_1\cos(q_1)-\cos(q_2)\sin(q_1-q_3)}{\sin(q_2-q_3)} & \frac{-l_1\cos(q_2)\sin(q_3-q_4)}{\sin(q_2-q_3)} \end{bmatrix}$.

To solve for the effective mass matrix of the system as seen at the end-effector, dynamic analysis is performed employing Lagrange's method. The kinetic co-energy T^* of the five-bar linkage is calculated as

$$\begin{aligned} T^* =& \tfrac{1}{24}m_1(k^2 + 4l_1^2)\dot{q}_1^2 + \tfrac{1}{24}(3m_1l_1^2 + m_4(k^2 + l_1^2))\dot{q}_4^2 \\ &+\tfrac{1}{24}m_2(k^2\dot{q}_2^2 + 4l_2^2\dot{q}_2^2 + 12l_1^2\dot{q}_1^2 + 12l_1l_2\cos(q_1 - q_2)\dot{q}_1\dot{q}_2) \\ &+\tfrac{1}{24}m_3(k^2\dot{q}_3^2 + 4l_2^2\dot{q}_3^2 + 12l_1^2\dot{q}_4^2 + 12l_1l_2\cos(q_3 - q_4)\dot{q}_3\dot{q}_4) \end{aligned} \tag{A.0.6}$$

Since the gravity acts out of the plane of the mechanism, the kinetic co-energy of the system is equal to the Lagrangian L of the system. Eliminating the dependent generalized velocities and invoking Lagrange's equation, the elements of the mass matrix D can be derived as

$D_{11} = \frac{1}{12}m_1(k^2 + 4l_1^2) + \frac{1}{12}m_3l_1^2\sin(q_1 - q_2)^2(4/\sin(q_2 - q_3)^2 + k^2/l_2^2/\sin(q_2 - q_3)^2) + \frac{1}{12}m_2l_1^2(12+k^2\sin(q_1-q_3)^2/l_2^2/\sin(q_2-q_3)^2+4\sin(q_1-q_3)(\sin(q_1-q_3)-3\sin(q_2-q_3)\cos(q_1-q_2))/\sin(q_2 - q_3)^2)$

$D_{12} = \frac{1}{12} l_1^2 (m_2 \sin(q_3 - q_4)(k^2 \sin(q_1 - q_3)/l_2^2/\sin(q_2 - q_3)^2 + (4\sin(q_1 - q_3) - 6\sin(q_2 - q_3)\cos(q_1 - q_2))/\sin(q_2 - q_3)^2) + m_3 \sin(q_1 - q_2)(k^2 \sin(q_2 - q_4)/l_2^2/\sin(q_2 - q_3)^2 + (4\sin(q_2 - q_4) - 6\sin(q_2 - q_3)\cos(q_3 - q_4))/\sin(q_2 - q_3)^2))$

$D_{22} = \frac{1}{4} m_1 l_1^2 + \frac{1}{12} m_4 (k^2 + l_1^2) + \frac{1}{12} m_2 l_1^2 \sin(q_3 - q_4)^2 (4/\sin(q_2 - q_3)^2 + k^2/l_2^2/\sin(q_2 - q_3)^2) + \frac{1}{12} m_3 l_1^2 (12 + k^2 \sin(q_2 - q_4)^2/l_2^2/\sin(q_2 - q_3)^2 + 4\sin(q_2 - q_4)(\sin(q_2 - q_4) - 3\sin(q_2 - q_3)\cos(q_3 - q_4))/\sin(q_2 - q_3)^2)$.

Finally, the effective mass matrix of the system as seen at the end-effector can then be calculated using the formula

$$M = J^{-T} D J^{-1}. \tag{A.0.7}$$

Appendix B

Implementation Details of the NBI method

Since the NBI method inherits the convergence properties of gradient-based techniques, some amount of tuning is required to achieve solutions in an effective manner. The following list presents the parameters that can be tuned and nominal values of these parameters that are used in this thesis.

1 **Discretization of the Workspace:** Since the objective functions require global search to be conducted for determining the extreme singular values over the entire workspace, discretization of the workspace has crucial effect on the accuracy of the global optima obtained. In other words, one can easily miss the exact global optimum due to course discretization of the workspace. On the other hand, very fine discretization leads to high computational load. In this study, $\pi/180$ rad is selected as the discretization step size for the workspace.

2 **Tolerance of the Constraint Functions:** Since the NBI method relies on an equality constraint for finding the furthest point on a line within the feasible objective space, tolerances of constraint functions directly affect the convergence of the method. Decreasing these tolerances may avoid converging to local optima at a cost of increasing the computational time. In this study, the tolerances on the design variables (TolX) are set to 10^{-6}, while the tolerances on objective functions (TolF) are set to 10^{-6}. Finally, the tolerance on the constraint functions (TolCon) is assigned as 10^{-8} for both the five bar and exoskeleton mechanisms.

3 **Number of Solutions in the Pareto-front Set:** Since the NBI method attacks the geometric problem directly by solving for single-objective constrained subproblems with a gradient based search algorithm, initialization of each subproblem has drastic effect on Pareto-front set obtained. Since initializations are directly related to the number of solutions determined by the user, the number of solutions also influence the convergence of solutions on Pareto-front hyper surface. In this study, the number of solutions in the Pareto-front set is set as 10 and 30.

4 **Order of Shadow Points:** The NBI method starts for searching the optimum solutions from one of the shadow points: hence, the order of the shadow points input to the algorithm has an effect on the initialization. It has been observed that changing the order of the shadow points can lead to better convergence behavior of the NBI method, while a "bad" initialization may not converge at all. In this study, the Pareto-front curve of the five bar mechanism is solved with the order of $\mathcal{GDI} \rightarrow \mathcal{GII}$, while the exoskeleton mechanisms used $\mathcal{GII} \rightarrow \mathcal{GDI}$as the ordering of the shadow points.

Bibliography

[1] G. Alici and B. Shirinzadeh. Optimum synthesis of planar parallel manipulators based on kinematic isotropy and force balancing. *Robotica*, 22(1):97–108, 2004.

[2] H. Asada. A geometrical representation of manipulator dynamics and its application to arm design. *ASME Journal of Dynamic Systems, Measurement, and Control*, 105(3):131–135, 1983.

[3] A.K. Bejczy and J. K. Salisbury. Controlling remote manipulators through kinesthetic coupling. *In ASME Computers in Mechanical Engineering*, 2(1):48–60, 1983.

[4] I. A. Bonev and C. M. Gosselin. Singularity loci of spherical parallel mechanisms. In *IEEE International Conference on Robotics and Automation*, pages 2957–2962, 2005.

[5] G. C. Burdea. *Force and Touch Feedback for Virtual Reality*. 1996.

[6] D. Chablat, P. Wenger, F. Majou, and J. Merlet. An interval analysis based study for the design and the comparison of 3-DoF parallel kinematic machines. *International Journal of Robotics Research*, 6(23):615–624, 2004.

[7] W. Chen, Q. Zhang, Z. Zhao, and W. A. Gruver. Optimizing multiple performance criteria in redundant manipulators by subtask-priority control. In *IEEE International Conference on Systems, Man and Cybernetics*, volume 3, pages 2534–2539, 1995.

[8] C. A. Coello. An updated survey of GA-based multiobjective optimization techniques. *ACM Computing Surveys*, 32(2):109–143, 2000.

[9] O. Kocak D. G. Caldwell and U. Andersen. Multi-arm dexterous manipulator operation using glove/exoskeleton control and sensory feedback. In *IEEE/RSJ International Conference on Intelligent Robots and Systems*, pages 567–572, 1995.

[10] I. Das and J. Dennis. A closer look at drawbacks of minimizing weighted sums of objectives for pareto set generation in multicriteria optimization problems. *Journal Structural and Multidisciplinary Optimization*, 14(1):63–69, 1997.

[11] I. Das and J. E. Dennis. Normal-boundary intersection: A new method for generating the pareto surface in nonlinear multi-criteria optimization problems. *SIAM Journal on Optimization*, 8(3):631–65, 1996.

[12] O. L. de Weck. Multiobjective optimization: History and promise. In *China-Japan-Korea Joint Symposium on Optimization of Structural and Mechanical Systems*, Invited Keynote Paper, 2004.

[13] R. Di Gregorio. Kinematics of a new spherical parallel manipulator with three equal legs: The 3-URC wrist. *Journal of Robotic Systems*, 18(5):213–219, 2001.

[14] C. M. Fonseca and P. J. Fleming. Genetic algorithms for multiobjective optimization: Formulation, discussion and generalization. In *Multiobjective evolutionary algorithms: Empirical Genetic Algorithms*, pages 416–423, 1993.

[15] R. Gillespie. On-line symbolic constraint embedding for simulation of hybrid dynamical systems. *Multibody System Dynamics*, 14:387–417(31), 2005.

[16] R.B. Gillespie. Kanes equations for haptic display of multibody systems. *Haptics-e, The Electronic Journal for Haptics Research*, 2(3), 18 August 2003 2003.

[17] C. Gosselin and J. Angeles. A global performance index for the kinematic optimization of robotic manipulators. *ASME Journal of Mechanical Design*, 113(3):220–226, 1991.

[18] A. Gupta and M. K. O'Malley. Design of a haptic arm exoskeleton for training and rehabilitation. *IEEE Transactions on Mechatronics*, 11(3), 2006.

[19] A. Gupta, V. Patoglu, M. K. O'Malley, and C. M. Burgar. Design, control and performance of RiceWrist: A force feedback wrist exoskeleton for rehabilitation and training. *International Journal of Robotics Research, Special Issue on Machines for Human Assistance and Augmentation*, to appear.

[20] V. Hayward, J. Choksi, G. Lanvin, and C. Ramstein. Design and multiobjective optimization of a linkage for a haptic interface. In *Advances in Robot Kinematics*, pages 352–359, 1994.

[21] C. Innocenti and V. Parenti-Castelli. Echelon form solution of direct kinematics for the general fully parallel spherical wrist. *Mechanisms and Machine Theory*, 28(4):553–561, 1993.

[22] H. Ishibuchi and K. Narukawa. Comparison of evolutionary multiobjective optimization with reference solution-based single-objective approach. In *Genetic and Evolutionary Computation*, pages 787–794, 2005.

[23] Dongshin C. Lee J-O. Park J-H. Park J. Choi, J. Kim. Design and characteristic analysis of 7 dof hybrid master arm woth human kinematics. In *ASME Dynamic Systems and Control Division, DSC-Vol. 64*, pages l95–205, 1998.

[24] Garcia De Jalon, Javier and Eduardo Bayo. *Kinematic and Dynamic Simulation of Multibody Systems: The Real-Time Challenge*. Springer Verlag, 1993.

[25] S. Joshi and L. W. Tsai. A comparison study of two 3-DoF parallel manipulators: one with three and the other with four supporting legs. *IEEE Transactions on Robotics and Automation*, 2(19):200–209, 2003.

[26] T. R. Kane. *Dynamics, Theory and Applications*. McGraw-Hill, New York, 1985.

[27] Thomas Kane and David A. Levinson. A multibody motion stability analysis. *Multibody System Dynamics*, 3:287–299, 1999.

[28] M. Karouia and J. M. Herve. A family of novel orinetational 3-DoF parallel robots. In *CISM-IFToMM Symposium on Robot Design, Dynamics, and Control*, pages 359–368, 2002.

[29] E. M. Kasprzak and K. E. Lewis. An approach to facilitate decision tradeoffs in Pareto solution sets. *Journal of Engineering Valuation and Cost Analysis*, 3(1):173–187, 2000.

[30] W. A. Khan and J. Angeles. The kinetostatic optimization of robotic manipulators: The inverse and the direct problems. *Transaction of ASME Journal of Mechanical Design*, 128(1):168–178, 2006.

[31] I. Y. Kim and O. L. de Weck. Adaptive weighted-sum method for bi-objective optimization: Pareto front generation. *Journal Structural and Multidisciplinary Optimization*, 29:149–158, 2005.

[32] X. Kong and C. M. Gosselin. Type synthesis of 3-DoF spherical parallel manipulators based on screw theory. In *ASME Design Engineering Technical Conferences*, 2002.

[33] M. Krefft and J. Hesselbach. Elastodynamic optimization of parallel kinematics. In *IEEE International Conference on Automation Science and Engineering*, pages 357–362, 2005.

[34] M. Krefft and J. Hesselbach. Elastodynamic optimization of parallel kinematics. In *IEEE International Conference on Automation Science and Engineering*, pages 357–362, 2005.

[35] M. Krefft, H. Kerle, and J. Hesselbach. The assesment of parallel mechanisms – it is not only kinematics. *Production Engineering*, 12(1):173–173, 2005.

[36] J. H. Lee, K. S. Eom, B-J. Yi, and I. H. Suh. Design of a new 6-DoF parallel haptic device. In *IEEE International Conference on Robotics and Automation*, volume 1, pages 886–891, 2001.

[37] K. M. Lee and D. K. Shah. Kinematic analysis of a three degrees-of-freedom in-parallel actuated manipulator. *IEEE Transactions on Robotics and Automation*, 4(3):354–360, 1988.

[38] S-U. Lee and S. Kim. Analysis and optimal design of a new 6-DoF parallel type haptic device. In *IEEE/RSJ International Conference on Intelligent Robots and Systems*, pages 460–465, 2006.

[39] Martin Lesser. A geometrical interpretation of Kane's equations. *Proceedings of the Royal Society of London, Series A.*, 436:69–87, 1992.

[40] C. H. Liu and S. Cheng. Direct singular positions of 3RPS parallel manipulators. *ASME Journal of Mechanical Design*, (126):1006–1016, 2004.

[41] X-J Liu and J. Wang. A new methodology for optimal kinematic design of parallel mechanisms. *Mechanism and Machine Theory*, 42:1210–1224, 2007.

[42] X-J Liu, J. Wang, and H-J Zheng. Optimum design of the 5R symmetrical parallel manipulator with a surrounded and good-condition workspace. *Robotics and Autonomous Systems*, 54(3):221–233, 2006.

[43] Y. Lou, G. Liu, and Z. Li. Randomized optimal design of parallel manipulators. *IEEE Transactions on Automation Science and Engineering*, to appear.

[44] G. Parrini F. Salsedo S. Scattareggia Marchese M. Bergamasco, D.M. De Micheli. Design considerations for glove-like advanced interfaces. In *In ICAR International Conferences on Advanced Robotics*, pages 2574–2579, 1998.

[45] S. McGhee, T. Fung Chan, R. V. Dubey, and R. L. Kress. Probability-based weighting of performance criteria for a redundant manipulator. In *ICRA*, pages 1887–1894, 1994.

[46] J.P. Merlet. *Parallel Robots*. Springer, second edition, 2006.

[47] R. S. Mosher. From handyman to hardiman. *Society of Automotive Engineers*, 76:588–597, 1967.

[48] G. A. Merdano-Cerda N. Tsagarakis, D. G. Caldwell. A 7 dof pneumatic muscle actuator powered exoskeleton. In *IEEE International Workshop on Robot and Human Interaction*, pages 327–333, 1999.

[49] L. Qi and R. S. Womersley. On extreme singular values of matrix valued functions. *Journal of Convex Analysis*, 3(1):153–166, 1996.

[50] E. Rigoni and S. Poles. NBI and MOGA-II, two complementary algorithms for multi-objective optimizations. In *Practical Approaches to Multi-Objective Optimization*, 2005.

[51] A. Risoli, G. M. Prisco, F. Salsedo, and M. Bergamasco. A two degrees-of-freedom planar haptic interface with high kinematic isotropy. In *IEEE International Workshop on Robot and Human Interaction*, pages 297–302, 1999.

[52] M. Kim C.W. Lee S. Lee, S. Park. Design of a force reflecting master arm and master hand using pneumatic actuators. In *IEEE International Conference on Robotics and Automation*, pages 162–167, 1991.

[53] J. K. Salisbury and J. J. Craig. Articulated hands: Force control and kinematic issues. *The International Journal of Robotics Research*, 1(1):4–17, 1982.

[54] Michael William Sayers. *Symbolic Computer Methods To Automaically Formulate Vehicle Simulation Codes*. PhD thesis, The University of Michigan, Ann Arbor, 1990.

[55] D. B. Schaechter and D. A. Levinson. Interactive computerized symbolic dynamics for the dynamicist. *Journal of Astronautical Sciences*, 36(4):365–388, Nov-Dec 1988.

[56] S-D. Stan, V. Maties, and R. Balan. Optimal design of 2 DoF parallel kinematics machines. In *Applied Mathematics and Mechanics*, pages 705–706, 2006.

[57] L. Stocco, S. E. Salcudean, and F. Sassani. Fast constrained global minimax optimization of robot parameters. *Robotica*, 16(6):595–605, 1998.

[58] B. Stuckman and E. Easom. A comparison of bayesian/sampling global optimization techniques. *IEEE Transactions of Systems, Man and Cybernetics*, 22(5):1024–1032, 1992.

[59] B. Stuckman, G. Evans, and M. Mollaghasemi. Comparison of global search methods for design optimization using simulation. In *IEEE Winter Simulation Conference*, pages 937–944, 1991.

[60] R. Unal, G. Kiziltas, and V. Patoglu. A multi-criteria design optimization framework for haptic interfaces. In *IEEE International Symposium on Haptic Interfaces for Virtual Environments and Teleoperator Systems*, 2008.

[61] R. Unal, G. Kiziltas, and V. Patoglu. Multi-criteria design optimization of parallel robots. In *IEEE International Conference on Cybernetics and Intelligent Systems and IEEE International Conference on Robotics, Automation and Mechatronics, CIS-RAM 2008*, page to appear, 2008.

[62] R. Unal and V. Patoglu. Optimal dimensional synthesis of a dual purpose haptic interface. In *Lecture Notes in Computer Science, Springer*, page to appear, 2008.

[63] R. Unal and V. Patoglu. Optimal dimensional synthesis of force feedback lower arm exoskeletons. In *IEEE RAS / EMBS International Conference on Biomedical Robotics and Biomechatronics, BioRob 2008*, page to appear, 2008.

[64] P. Wenger, C. Gosselin, and D. Chablat. A comparative study of parallel kinematic architectures for machining applications. In *Proceedings of the Workshop on Computational Kinematics*, pages 249–258, 2001.

[65] K. Kim Y.S. Hong-J.O. Park Y. Jeong, Y. Lee. A 7 dof wearable robotic arm using pneumatic actuators. In *Proceedings of the 32nd ISR, International Symposium on Robotics*, 2001.

[66] G. Yang, H. L. Ho, W. Chen, W. Lin, S. H. Yeo, and M. S. Kurbanhusen. A haptic device wearable on a human arm. In *IEEE Conference on Robotics, Automation and Mechatronics*, pages 243–247, 2004.

[67] G. Yang, W. Lin, M. S. Kurbanhusen, C. B. Pham, and S. H. Yeo. Kinematic design of a 7-dof cable-driven humanoid arm: a solution-in-nature approach. In *IEEE/ASME Conference on Advanced Intelligent Mechatronics*, pages 444–449, 2005.

[68] J. Yoon and J. Ryu. Design, fabrication, and evaluation of a new haptic device using a parallel mechanism. *IEEE/ASME Transactions on Mechatronics*, 6(3):221–233, 2001.

[69] T. Yoshikawa. Dynamic manipulability of robotic mechanisms. *Journal of Robotic Systems*, 2(1):113–123, 1985.

[70] S. Lee M. Kim Y.S. Kim, J. Lee. A force reflected exoskeleton-type master arm for human robot interaction. *IEEE Transactions on Systems, Man, and Cybernetics, Part A*, 35(2):198–212, 2005.

[71] Y. Zheng and W.L. Lewis. Several algorithms of global optimal search. *Advances in Enginering Software*, 22(2):87–98, 1994.

[72] E. Zitzler, K. Deb, and L. Thiele. Comparison of multiobjective evolutionary algorithms: Empirical results. *Evolutionary Computation*, 8(2):149–172, 2000.